J. Fluid Mech. (2002), *vol.* 462, *pp.* 307–340.
DOI: 10.1017/S0022112002008339 Printed in the United Kingdom

Life of a smooth liquid sheet

By CHRISTOPHE CLANET
AND EMMANUEL VILLERMAUX

Institut de Recherche sur les Phénomènes Hors Equilibre, UMR 6594, Technopôle de Château Gombert, 49 rue F. Joliot-Curie-BP146, 13384 Marseille cedex 13, France

(Received 13 September 2000 and in revised form 14 January 2002)

We report on experiments with liquid sheets formed through the impact of a slender jet on a small disc at high Reynolds number. When the interaction with the surrounding air is negligible, the sheet spreads out radially and remains smooth. The study extends over the whole life of the sheet, considering the dynamics of its formation and destruction and paying special attention to the stationary regime, in which the transition from sheet to drops occurs.

1. Introduction

In 1833 Savart published experimental results on several open problems involving liquid jets:

the structure of liquid jets coming out of a circular hole in a thin wall (1833*a*);

liquid jet impact on a circular solid surface (1833*b*, *c*);

the impact of two liquid jets facing one another (1833*d*).

Among all the observations and questions opened by this major pioneering work, we focus here on the impact of two liquid jets facing one another, which is equivalent, in the non-viscous limit, to the problem presented in figure 1(*a*). The vertical jet of diameter D_0, impacts with velocity U_0 a small horizontal disc of diameter D_i, and the resulting film is forced to spread out radially with ejection angle $\psi_0 = \pi/2$. In this configuration, the liquid sheet extends radially to a critical location R, where it disintegrates into droplets. If the Froude number $Fr_R \equiv gR/U_0^2$, based on the acceleration due to gravity g, is small compared to unity, the effect of this acceleration on the fluid particle trajectory can be neglected and the liquid sheet remains flat.

Depending on the Weber number, $We \equiv \rho U_0^2 D_0/\sigma$, based on the liquid density ρ and surface tension σ, two distinct regimes can be identified:

(i) A smooth regime is observed in the range $We < We_c$, where We_c is a critical Weber number of the order of 10^3. In this regime, the action of the surrounding air on the dynamics of the sheet can be neglected, and the liquid sheet remains smooth and planar up to the edge as illustrated in figures 1(*b*) and 1(*c*).

(ii) A flapping regime is observed at higher Weber numbers $We > We_c$, where the edge of the sheet is moving up and down like a flag flapping in the wind (figure 1*d*).

Both regimes were noticed by Savart during his study of the impact of two water jets of diameter 3 mm facing one another with a jet spacing of 3 cm: "for all the pressure tested (from few centimeters to 488 cm of water column), a flat and circular liquid sheet was formed at the meeting point of the two jets in a plane orthogonal to the jet axis. This liquid sheet was observed to be thicker in its central part than at the periphery and to terminate in a blurred, rough and noisy region when the pressure exceeds 120 cm of water. For lower pressures, the liquid sheet is smooth

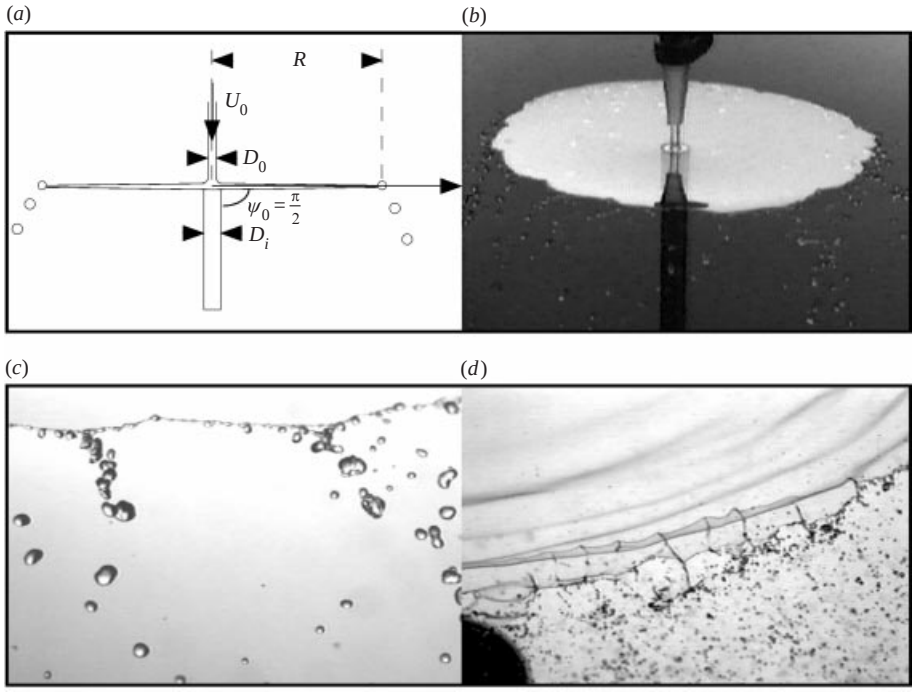

FIGURE 1. Presentation of the experiment: (*a*) diagram, (*b*) side view for $We = 510$, (*c*) close-up view of the edge of the sheet for $We = 510$, (*d*) close-up view of the edge of the sheet for $We = 3000$.

and transparent over the whole diameter". For the radial extension R in the smooth regime, Savart summarizes his observations in two points:

the diameter of the smooth liquid sheet is proportional to the pressure;

the diameter of the liquid sheet is proportional to the exit cross-section area, at least for the smaller pressures.

These observations have motivated a large number of studies. From Bouasse (1923), we learn that the facing jet impact was studied by Plateau (1873) and Hagen. The observations of Savart on the smooth regime are also the starting point of the work of Taylor (1959*a–c*). According to Taylor, the sheet radius should vary as

$$\frac{R}{D_0} = \frac{We}{16}. \tag{1.1}$$

This law is fully compatible with Savart's observations. In an experiment with two facing jets similar to that by Savart, Huang (1970) has shown that for the water/air system, this law holds up to a critical Weber number $We_c \simeq 10^3$. For higher Weber numbers, Huang reports the radius evolving as $R/D_0 \sim We^{-1/3}$, compatible with the *flag* instability described by Squire (1953) for a uniform liquid sheet and extended to a radially expanding liquid sheet by Weihs (1978). A detailed study of this flag instability regime observed at high Weber numbers is reported in Villermaux & Clanet (2002).

We focus here on the smooth regime, where $R \approx WeD_0/16$. The low-gravity domain defined by $gR/U_0^2 \ll 1$ can thus be expressed as $(D_0/a) \ll 2\sqrt{2}$, where $a \equiv \sqrt{2\sigma/(\rho g)}$, is the capillary length of the liquid–air interface. The ratio D_0/a is usually referred to as the Bond number, Bo. In the (Bo, We)-plane, the domains corresponding to the smooth and flapping regimes are presented in figure 2. The minimum Weber number

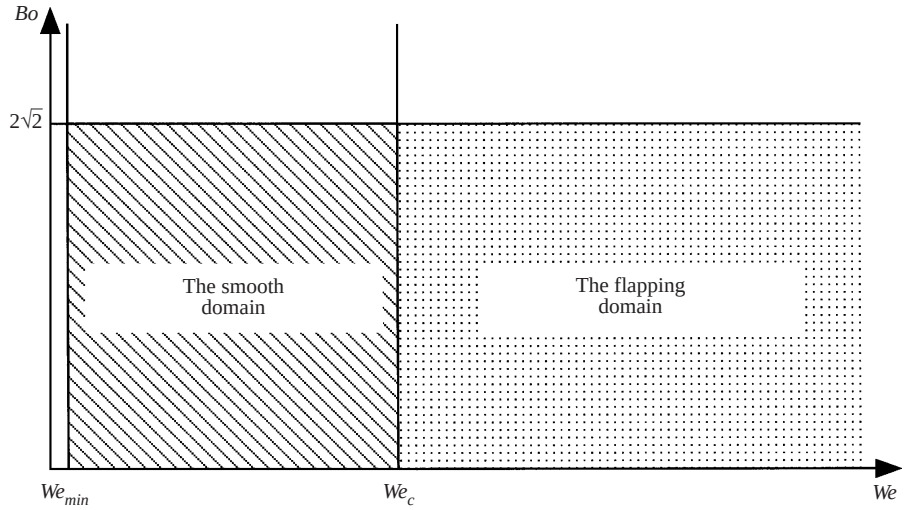

FIGURE 2. Presentation in the (Bo, We)-plane of the smooth regime domain considered in this study and of the flag instability domain considered in Villermaux & Clanet (2002).

We_{min} which bounds the first domain corresponds to the limit of detachment of the jet from the impactor. This detaching problem is discussed in Clanet (2001). It is also important to note that the study is conducted only on laminar jets.

In this study, we first analyse the structure of the liquid sheet in terms of its local velocity and thickness in the stationary regime. The dynamics of its formation and destruction is then studied, prior to the drop formation mechanism at the edge. This topological evolution from sheet to drops often occurs in atomization processes, e.g. Dombrowski & Fraser (1954), Bayvel & Orzechowski (1993), and remains poorly understood. To improve its understanding, Savart's configuration presents the advantages that it is stationary and has a reduced number of control parameters. In this respect, it can be compared to the rotating cup configuration studied by Hinze & Milborn (1950) and Fraser, Dombrowski & Routley (1963).

Section 2 describes the experimental set-up used to produce and study the liquid sheets. The experimental results and the models are respectively presented in § 3 and § 4, prior to the conclusion in § 5.

2. Experimental set-up

The experimental set-up is presented in figure 3(a). The Newtonian liquid, characterized by its density ρ, surface tension σ and kinematic viscosity v, is initially contained in a pressurized reservoir with a pressure P of the order of 2 to 3 bars. The experiment is in a closed loop to keep the characteristics of the fluid constant and also to allow the use of different fluids. When the reservoir is almost empty, the experiment is stopped and the reservoir is filled up via a peristaltic pump. The experiments reported have been conducted with water and ethanol, the properties of which are summarized in table 1, where the last column, a, is the capillary length. At the reservoir exit, two flow meters (AALBORG), in a parallel set-up allow control of the flow from $0.2\,\mathrm{cm^3\,s^{-1}}$ to $70\,\mathrm{cm^3\,s^{-1}}$ with a graduation resolution of $0.2\,\mathrm{cm^3\,s^{-1}}$. This enables an accurate control of the jet velocity U_0, defined as the ratio of the flow rate to the exit section area. Since the Froude number, $Fr_h = gh/U_0^2$, based on

Fluid	$\rho\,(\mathrm{kg\,m^{-3}})$	$\nu\,(\mathrm{m^2\,s^{-1}})$	$\sigma\,(\mathrm{kg\,s^{-2}})$	$a\,(\mathrm{m})$
Water	1000	10^{-6}	0.073	3.8×10^{-3}
Ethanol	810	1.5×10^{-6}	0.025	2.5×10^{-3}

TABLE 1. Physical properties of water and ethanol at 22°C.

$D_0\,(\mathrm{mm})$	$D_i\,(\mathrm{mm})$	D_i/D_0	Fluid	D_0/a
0.8	3.8	4.75	Water	0.21
0.8	3.8	4.75	Ethanol	0.32
2.7	10.8	4	Water	0.71
3.0	7.0	4	Water	0.79
2.7	10.8	4	Ethanol	1.08
5	20.8	4.2	Water	1.31

TABLE 2. Jet and impactor diameters with water and ethanol.

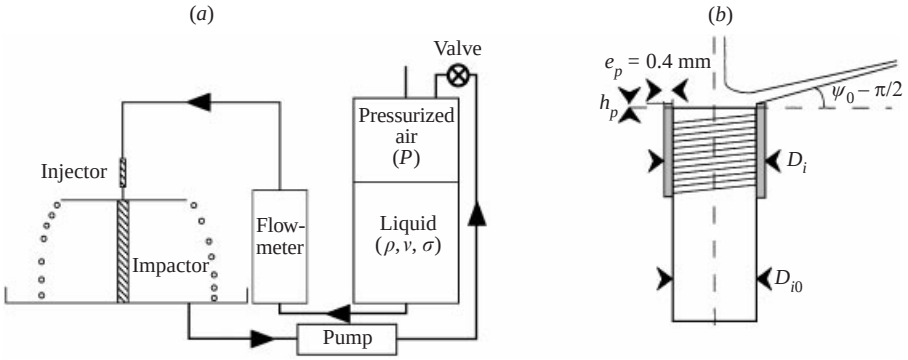

FIGURE 3. (*a*) Diagram of the experimental set-up. (*b*) The impactor, with the forcing device used to obtain $\psi_0 = \pi/2$

the distance, h, from the nozzle to the impactor never exceeded 10^{-2}, the contraction and acceleration of the jet prior to the impact is neglected herein.

The geometrical properties of the remaining two control parameters, D_0 and D_i, are presented in table 2. Three different nozzles are used to vary D_0 from 0.8 mm to 5.0 mm. The 0.8 mm jet is obtained with a thin wall hole of diameter $D = 1$ mm, which leads to an effective jet diameter $D_0 \simeq 0.8D$.† The 2.7 mm and 3.0 mm jets were created with a conical contraction, 25 mm long and 20 mm wide at the base, which ensures a contraction factor in cross-sectional area of the order of 50. The 5 mm jet was obtained with a convergent nozzle providing a contraction factor of 100. In all three cases, the velocity profile at the nozzle exit was close to top hat, and the jet remained laminar up to Reynolds numbers of the order of $Re \approx 30\,000$.

The impactor is a ground stainless steel cylinder with a carefully prepared upper surface of diameter $D_{i0} = 3$ mm, 10 mm, 6.2 mm and 20 mm respectively used with the 0.8 mm, 2.7 mm, 3.0 mm and 5 mm jets. The sheet was forced to exit the impact surface with the ejection angle $\psi_0 = \pi/2$ by means of a thin copper coaxial cylinder shown on figure 3(*b*). The thickness of this jacket is $e_p = 0.4$ mm, so that the impactor diameter

† The theoretical derivation of the contraction coefficient for thin holes $D_0/D = \sqrt{\pi/(\pi+2)}$ is due to Kirchhoff (1876).

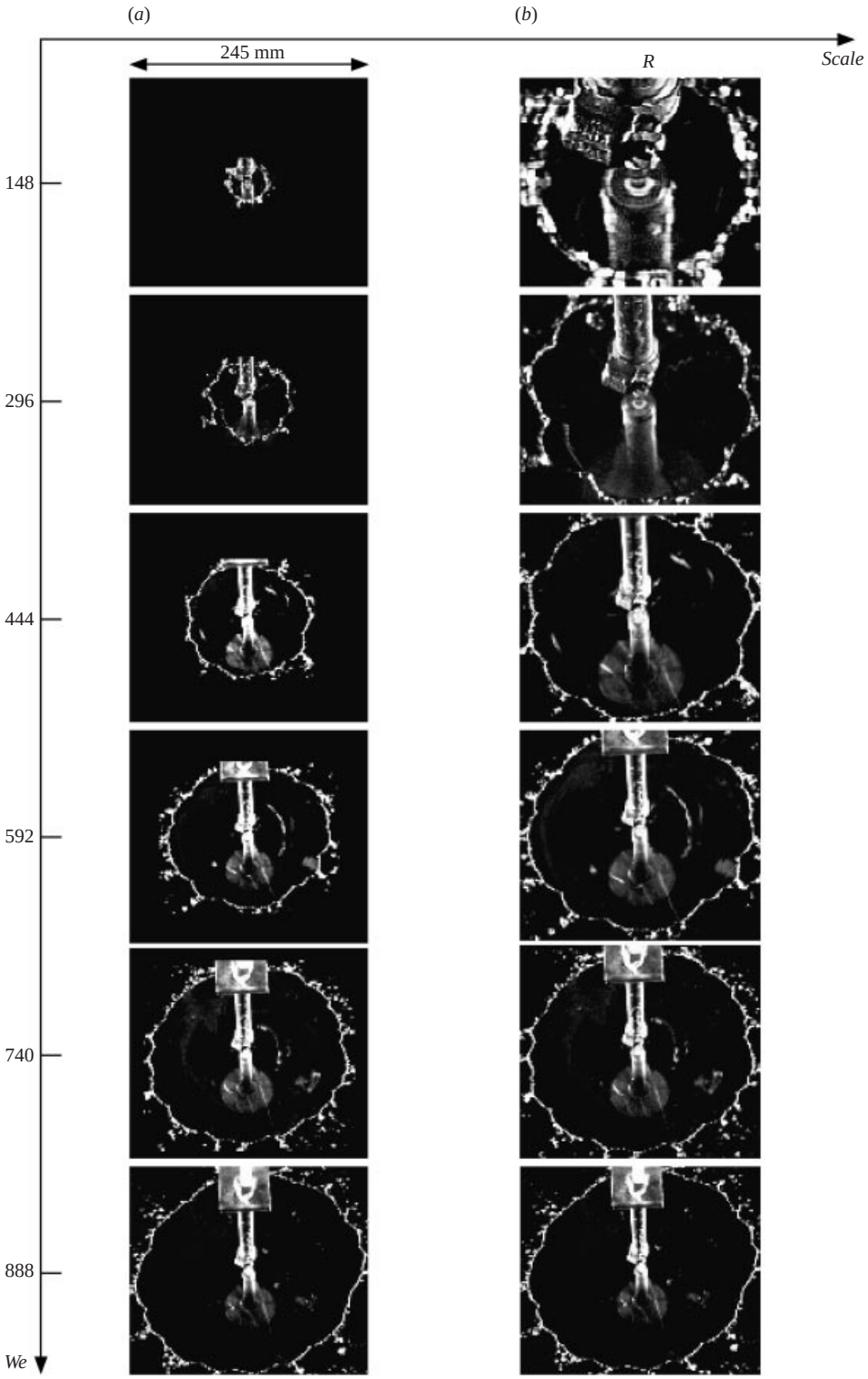

FIGURE 4. Qualitative presentation of the effect of the Weber number on the liquid sheet size and shape. The liquid is water and the jet and impactor are characterized by $D_0 = 2.7\,\text{mm}$ and $D_i = 10.8\,\text{mm}$. (*a*) Actual scale, (*b*) scaled by R.

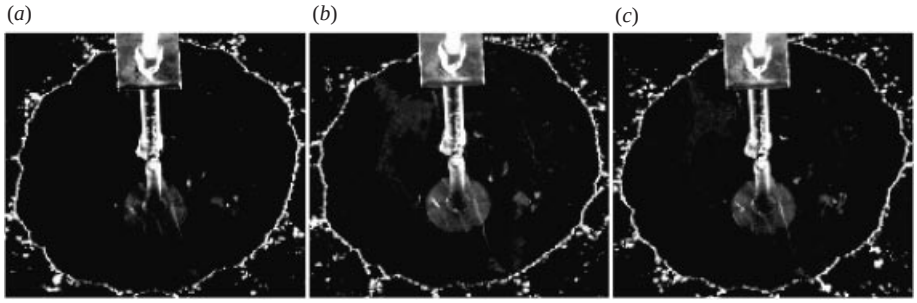

FIGURE 5. Qualitative presentation of the number and location of the indentations at the periphery of the sheet. The liquid is water and the jet and impactor are characterized by $D_0 = 2.7\,\text{mm}$ and $D_i = 10.8\,\text{mm}$. The Weber number on the three images is $We = 888$, and only the time at which the picture is taken changes.

seen by the jet is $D_i = D_{i0} + 2e_p$. The jet and impactor properties are summarized in table 2.

3. Experimental results

The presentation of our experimental results starts with a qualitative description of the influence of the Weber number on the size of the liquid sheet and the diameter of the drops. This is followed by a quantitative second stage in which the results are presented in five subsections: the control of the ejection angle, the evolution of the liquid sheet radius, the dynamics of its formation and destruction, the shape of the cusps observed at the periphery of the sheet, and finally to the drop formation and size.

3.1. *A qualitative overview*

The influence of the Weber number on the size and shape of the liquid sheet is presented in figure 4. This sequence is obtained with water and the jet and impactor used are characterized by $D_0 = 2.7\,\text{mm}$ and $D_i = 10.8\,\text{mm}$. For each picture, the flow is first established at the desired flow rate and the ejection angle fixed at $\pi/2$ using the lip of controllable height presented in figure 3(b). The camera is positioned above the sheet, slightly off centre, which is why in some of the images the circular sheet appears slightly elliptical. The sheet is illuminated symmetrically by two halogen lamps, so that mainly the edges of the liquid sheet appear on the pictures, the liquid sheet being transparent.

In figure 4(a) the scale is the same for all the images and it shows, in the vertical direction, the increase of the sheet radius when the Weber number is increased from 148 to $n \times 148$ with $n = \{2, 3, 4, 5, 6\}$. It can be seen that the factor 6 increase in the Weber number also leads to a factor close to 6 increase in the size of the sheet with a quasi-linear evolution.

In figure 4(b), the same images are presented on the scale R, so that the size of the sheet is the same on each picture. This reveals some indentations at the periphery of the sheet, the number of which seems to increase with the Weber number. An important remark on these indentations is that, for a given Weber number, their number is not constant and their locations are not stationary but change with time. We illustrate these two points in figure 5, where we present, using the same jet and impactor as in figure 4, three pictures obtained at different times, with the same Weber number, $We = 888$. Looking for example at the east pole of each picture, one

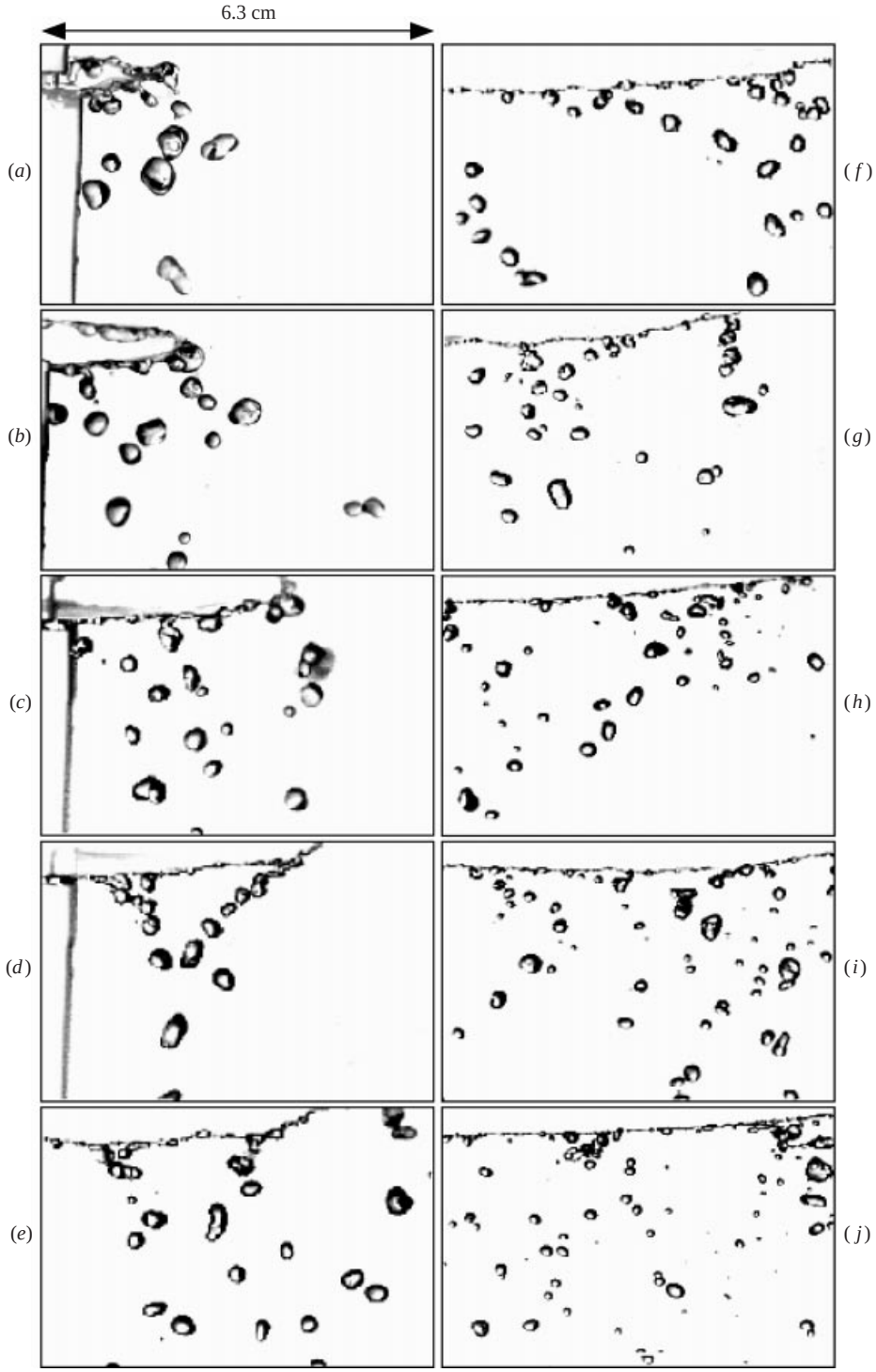

FIGURE 6. Qualitative presentation of the influence of the Weber number on the drops size: the liquid is water and the jet and impactor are characterized by $D_0 = 2.7\,\text{mm}$ and $D_i = 10.8\,\text{mm}$: (*a*) $We = 148$, (*b*) $We = 214$, (*c*) $We = 296$, (*d*) $We = 388$, (*e*) $We = 497$, (*f*) $We = 590$, (*g*) $We = 752$, (*h*) $We = 896$, (*i*) $We = 1060$, (*j*) $We = 1230$.

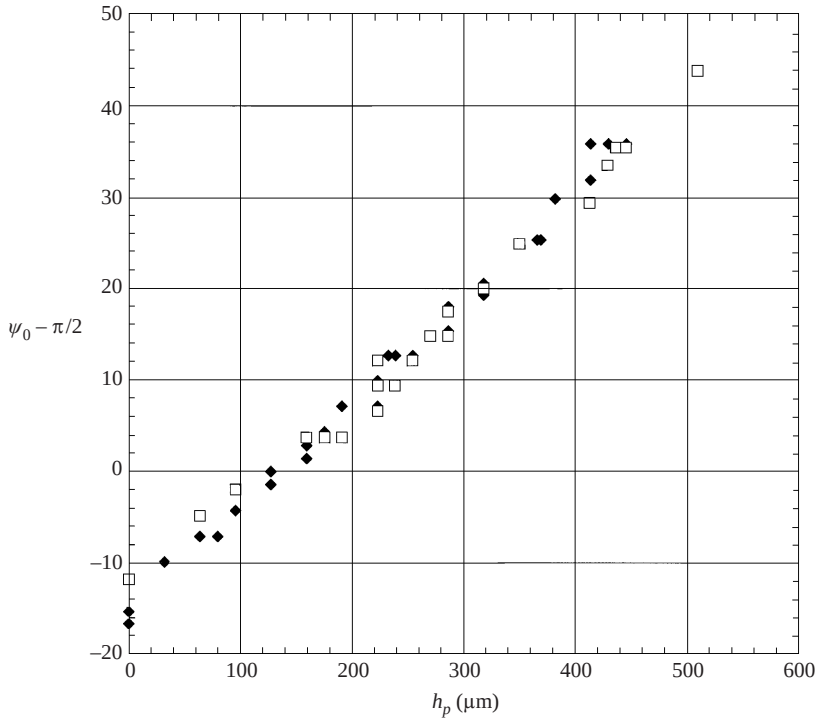

FIGURE 7. Evolution of the ejection angle ψ_0 with the height h_p of the coaxial cylinder ($D_0 = 3\,\text{mm}$, $D_i = 7\,\text{mm}$, $We = 300$): ◆, water; □, ethanol.

observes no indentation in (*a*), almost two in (*b*) and one in (*c*). This illustrates that the locations of the indentations change with time. Their number is not easy to count and, depending on the way the observation is done, the number of indentations on the three pictures can vary from 11 to 15.

The effect of the Weber number on the size of the drops produced by the disintegration of the sheet is presented in figure 6. The scale is the same in all the images and one can observe that the mean drop diameter decreases as the Weber number increases. Comparing figure 6(*a*) to 6(*j*), we find that an increase of the Weber number by a factor of 8.3 leads to a mean drop diameter decrease of the order of 2. We can also see in figure 6 the poly-disperse character of the drop size distribution. This does not affect the mean drop size definition, but rather provides information on the nature of the drop formation mechanism.

3.2. *Control of the ejection angle, ψ_0*

The ejection angle presented in figures 1(*a*) and 3(*b*) results from the local equilibrium of the liquid sheet at the edge of the impactor. For a flat impactor, $h_p = 0$, the sensitivity of this angle to both the diameter ratio D_i/D_0 and the impact Reynolds and Weber numbers is reported in Clanet (2001). One conclusion of that paper is that one cannot attain an angle of ejection $\psi_0 = \pi/2$ with a flat impactor. We have thus added the lip of controllable height, h_p, presented in figure 3(*b*), to overcome this limitation and we concentrate, here, on the influence of the lip on the ejection angle.

The evolution of $\psi_0(h_p) - \pi/2$ is reported in figure 7 for water and ethanol at $We = 300$ with $D_0 = 3\,\text{mm}$ and $D_i = 7\,\text{mm}$. From figure 7, $\psi_0 - \pi/2$ increases with h_p, starting at negative values for $h_p = 0$. Within the experimental accuracy,

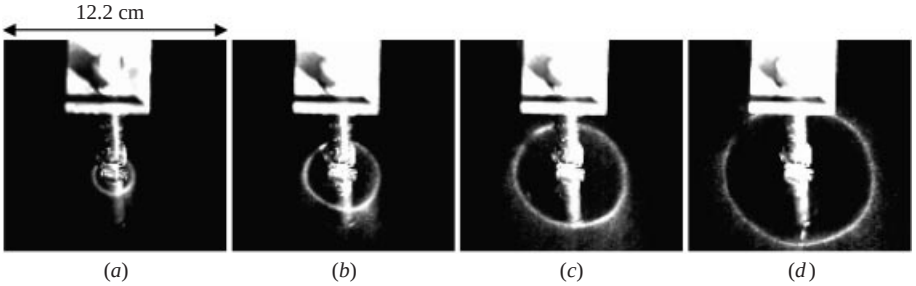

FIGURE 8. Average images obtained with water, $D_0 = 2.7$ mm, $D_i = 10.8$ mm. These images are used to determine the maximal extension, R: (*a*) $We = 96$, (*b*) $We = 153$, (*c*) $We = 225$, (*d*) $We = 311$.

the evolution of ψ_0 is the same for water and ethanol, at the same Weber number $We = 300$. For both liquids, the flat sheet corresponding to $\psi_0 - \pi/2 = 0$, is obtained for $h_p = h_p^\star \simeq 140\,\mu$m.†

3.3. *Evolution of the liquid sheet radius, R*

When the liquid sheet is forced to leave the impactor with the ejection angle $\psi_0 = \pi/2$, it spreads radially to the location R, where it disintegrates into droplets. The determination of R with an accuracy of the order of 5% is achieved using averaged images such as the one presented in figure 8.

The resulting evolution of the non-dimensional sheet diameter $2R/D_0$ is presented in figure 9 as a function of the Weber number, for the different jets, impactors and fluids: up to a critical Weber number $We_c \simeq 1200$, the liquid sheet diameter increases almost linearly with the Weber number and decreases above this limit. The scattering of our experimental data in the linear region will be shown in § 4 to be function of the losses on the impactor. These two characteristic trends of the evolution $2R/D_0 = f(We)$, are similar to those observed by Savart (1833*d*) and Huang (1970) in the case of the impact of two facing jets: a more quantitative comparison with their results is presented in the model section.

3.4. *Dynamics of the liquid sheet formation and destruction*

3.4.1. *Liquid sheet formation*

An example of sheet formation, observed with a high-speed video camera (Kodak HS4540), is presented in figure 10. In this figure, time increases from left to right and from top to bottom with a time step $\Delta t = 1/225$ s. The experimental procedure was as follows: the water jet is initially established at the desired flow rate, here $U_0 = 2.96\,\mathrm{m\,s^{-1}}$ ($We = 375$), and we use a hollow plastic tube to direct its trajectory away from the impactor. When the setting up of the camera is completed, the plastic tube is removed and we observe the impact of the jet on the disc. The main drawback of this procedure is that the leading edge of the jet is initially roughly defined as can be seen in the first images of the sequence. However, this procedure ensures that the jet velocity and diameter both remain constant over the whole formation process and allows a reasonable definition of the edge of the liquid sheet outside the impactor.

In the sequence presented in figure 10, the maximal extension $R = 5.7$ cm is reached

† Each time we change the impact Weber number, $h_p^\star$ has to be slightly modified so as to keep $\psi_0 = \pi/2$. However, the accuracy of our set-up (of the order of 20 μm) does not allow an accurate measurement of this sensitivity $h_p^\star(We)$.

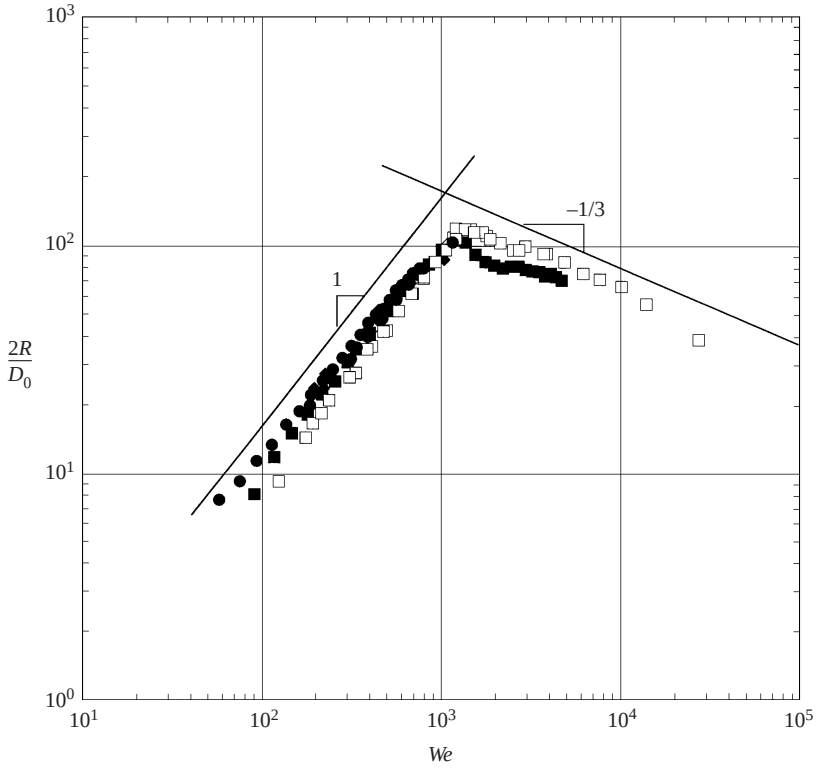

FIGURE 9. Evolution of the critical radius $2R/D_0$ with the impact Weber number: ◆, Injector 1 and water; ◇, $D_0 = 0.8$ mm, $D_i = 3.8$ mm and ethanol; ■, $D_0 = 2.7$ mm, $D_i = 10.8$ mm and water; □, Injector 2 and ethanol ●, $D_0 = 5$ mm, $D_i = 20.8$ mm and water.

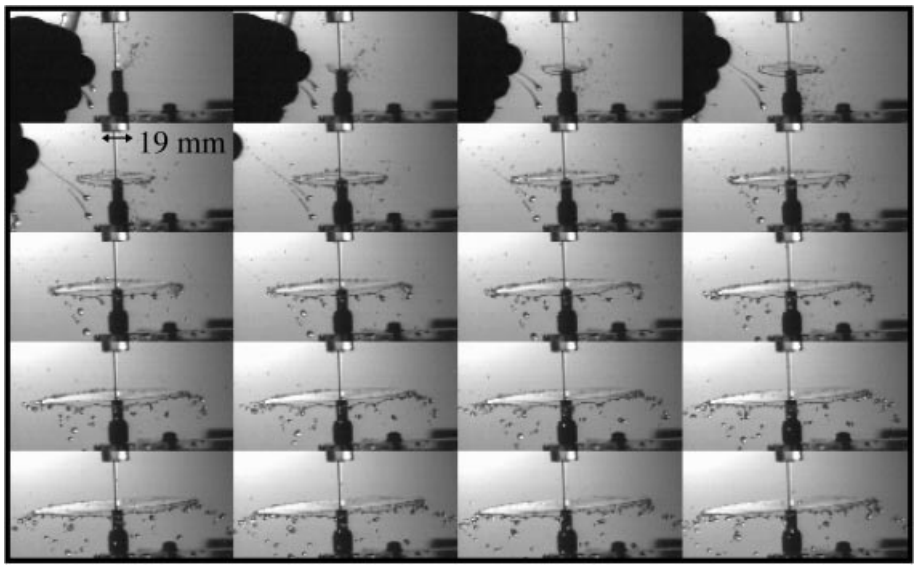

FIGURE 10. Dynamics of formation of a liquid sheet obtained with water, $D_0 = 3$ mm, $D_i = 7$ mm and $We = 375$. Time increases from left to right and from top to bottom with a time step $\Delta t = 1/225$ s.

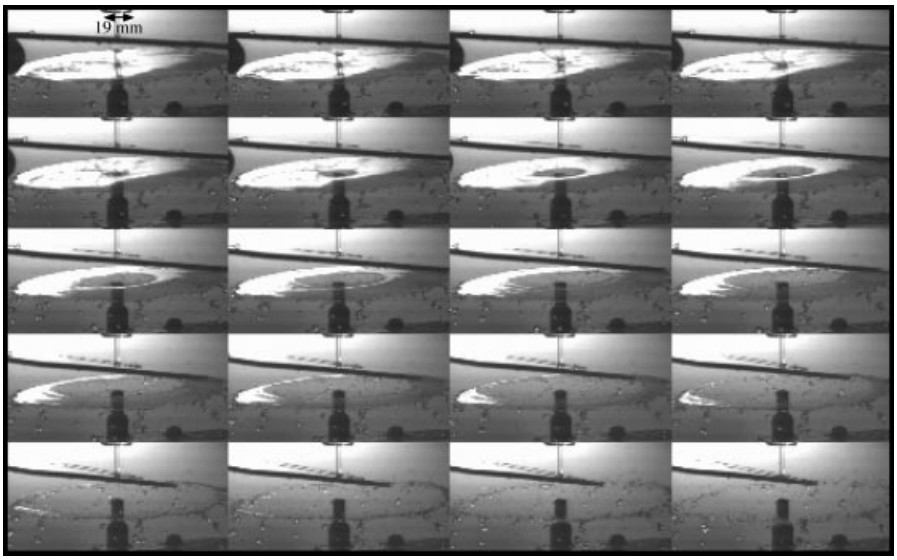

FIGURE 11. Dynamics of destruction of a liquid sheet obtained with water, $D_0 = 3\,\text{mm}$, $D_i = 7\,\text{mm}$ and $We = 410$. Time increases from left to right and from top to bottom with a time step $\Delta t = 1/1000\,\text{s}$.

in the last picture, at $t = 19\Delta t \approx 85\,\text{ms}$. This time is much larger than the transit time $T_t \equiv R/U_0 \approx 19\,\text{ms}$. Although R is reached at $t = 85\,\text{ms}$, the mid-point $R/2 = 2.85\,\text{cm}$ is reached much sooner, at $t = 4.5\Delta t \approx 20\,\text{ms}$. Both observations show that the edge of the sheet is moving relative to a liquid particle in the sheet with a velocity directed towards the impact point of the jet, a relative velocity which increases with the radial location of the edge.

3.4.2. *Liquid sheet destruction*

An example of sheet destruction is presented in figure 11. In this case, a stationary water sheet is first established at the desired conditions, here $U_0 = 3.1\,\text{m}\,\text{s}^{-1}$ and $We = 410$. Once the setting up of the camera is completed, we use a flat rigid device to cut and deviate the jet. The liquid sheet is then seen to open.

The first striking observation is that the outer edge of the sheet does not move during the opening process, so that the study of the sheet destruction reduces to the dynamics of the hole opening. In this sequence, $t = 0$ is defined in the top right image, when the cut part of the jet touches the impactor. The hole then starts to open and reaches the maximal extension $R = 6.5\,\text{cm}$, at $t = 14\Delta t \approx 14\,\text{ms}$, which is smaller than the transit time $T_t \equiv R/U_0 \approx 21\,\text{ms}$. The mid-point distance $R/2 = 3.25\,\text{cm}$, is reached at $t = 7\,\text{ms}$. Both observations show that the edge of the hole moves relative to the liquid in the remaining part of the sheet with a velocity directed towards the outer edge of the sheet, a relative velocity which remains almost constant.

3.5. *Shape of the cusps observed at the periphery of the sheet*

In the stationary regime, the indentations or cusps that appear naturally at the edge of the liquid sheet in the smooth regime are illustrated in figures 4 and 5. The evolution of the number of cusps N_c with the Weber number is presented in figure 12, for the experiments presented in figure 4, obtained with water, $D_0 = 2.7\,\text{mm}$ and $D_i = 10.8\,\text{mm}$. We observe that the number of cusps increases with the Weber

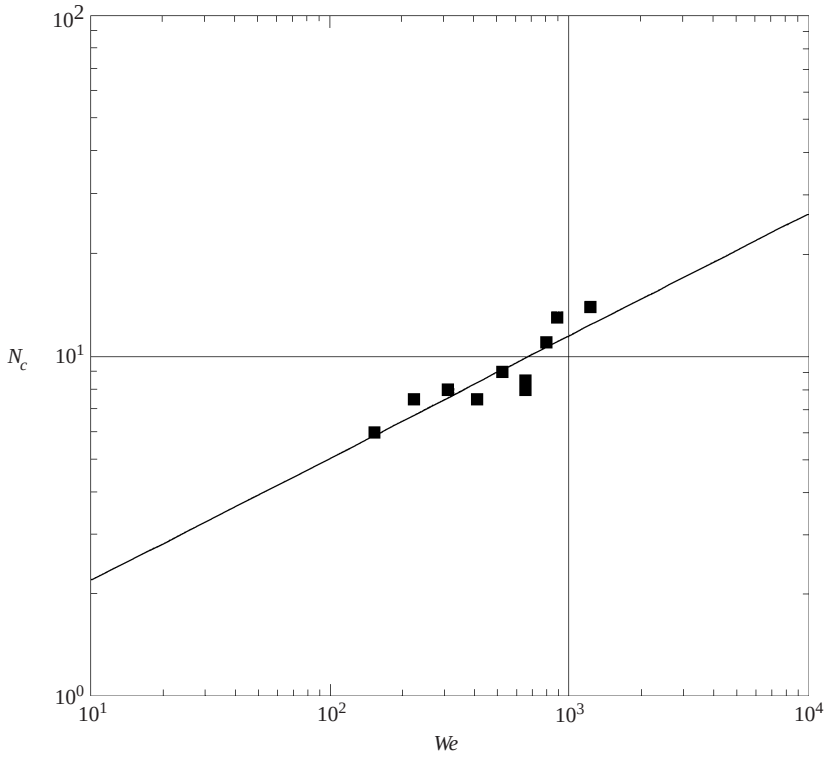

FIGURE 12. Evolution of the number of cusps with the Weber number: water is used with $D_0 = 2.7\,\text{mm}$ and $D_i = 10.8\,\text{mm}$.

number, and on the log-log scale the 'best fit' power law is $N_c \sim We^{0.36}$. However, due to the constant fluctuation of N_c, and to the difficulties of observation, one has to be cautious with this fit and should only consider it as an approximation.

These natural cusps can be forced, for example by cutting the sheet with a 80 μm tungsten wire coated with silicon oil. An example of a forced cusp observed by Savart is presented in figure 13. Quantitatively, we present in figure 14 the evolution of the cusp shape with the radial location of the wire r_0, which starts at the edge of the impactor, $r_0 = D_i/2$, and moves to the periphery of the liquid sheet, $r_0 = R$. This example is obtained with water, $D_0 = 2.7\,\text{mm}$, $D_i = 10.8\,\text{mm}$ and $We \simeq 1190$. In the figure, all the lengths are non-dimensionalized with the maximal radial extension $R = 13.5\,\text{cm}$, so that the location of the wire $\tilde{r}_0 \equiv r_0/R$, varies from 0.62 to 0.08. When the radial extent of the cusp reaches the location R, it disintegrates into droplets. A rim can be observed at the edge of the liquid sheet (figure 1*c*) which can be characterized by its mean diameter, D_{rim}. The evolution of the rim diameter D_{rim} and the drop diameter d are reported in figure 15 and compared to the injection diameter D_0, for two different Weber numbers $We = 1190$ and $We = 362$. The first observation from figure 15 is that the drop and rim diameters evolve similarly as the wire location is varied. For $We = 362$, the drop diameter is twice the rim diameter and remains almost constant, of the order of D_0, for the different wire locations. For $We = 1190$, the drop diameter is of the order of D_0 for cusp locations close to $r_0 = 0$ and decreases continuously down to $d \simeq 0.65D_0$ at $\tilde{r}_0 \simeq 1$. The ratio d/D_{rim} of the drop to rim diameter is 2 for $\tilde{r}_0 \simeq 0.05$ and increases to about 3 for $\tilde{r}_0 \simeq 1$. In both

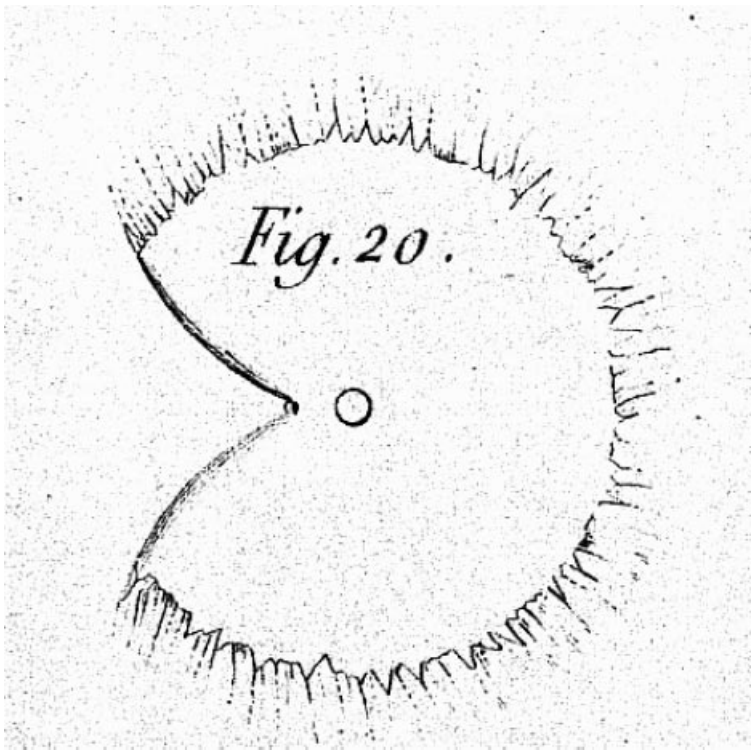

FIGURE 13. Upper view of a forced cusp from Savart Planche 4 (1833*d*).

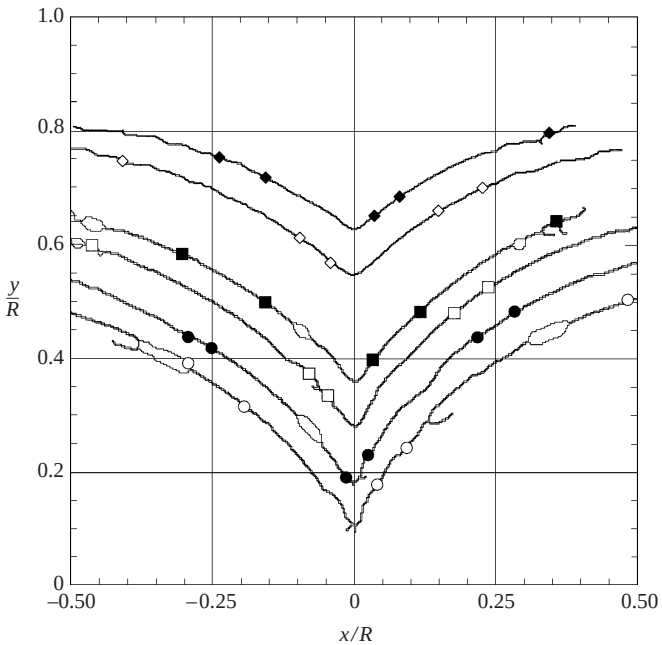

FIGURE 14. Evolution of the shape of the cusp with the wire location, $D_0 = 2.7$ mm, $D_i = 10.8$ mm and $We \simeq 1190$: ◆, $\tilde{r}_0 = 0.62$; ◇, $\tilde{r}_0 = 0.53$; ■, $\tilde{r}_0 = 0.35$; □, $\tilde{r}_0 = 0.27$; ●, $\tilde{r}_0 = 0.16$; ○, $\tilde{r}_0 = 0.08$.

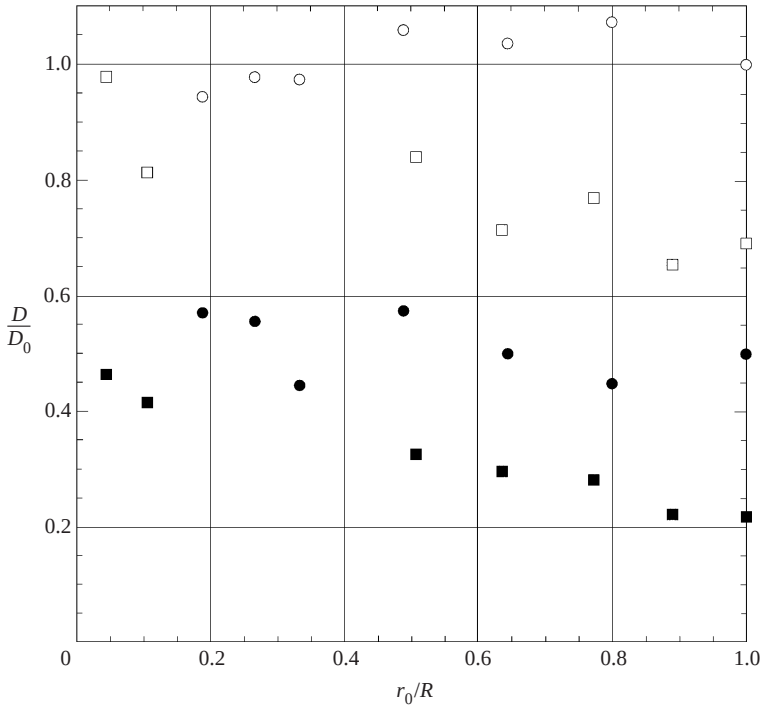

FIGURE 15. Rim and drop size evolution with the position of the wire: ■, D_{rim}/D_0 for $We = 1190$; □, d/D_0 for $We = 1190$; ●, D_{rim}/D_0 for $We = 362$; ○, d/D_0 for $We = 362$.

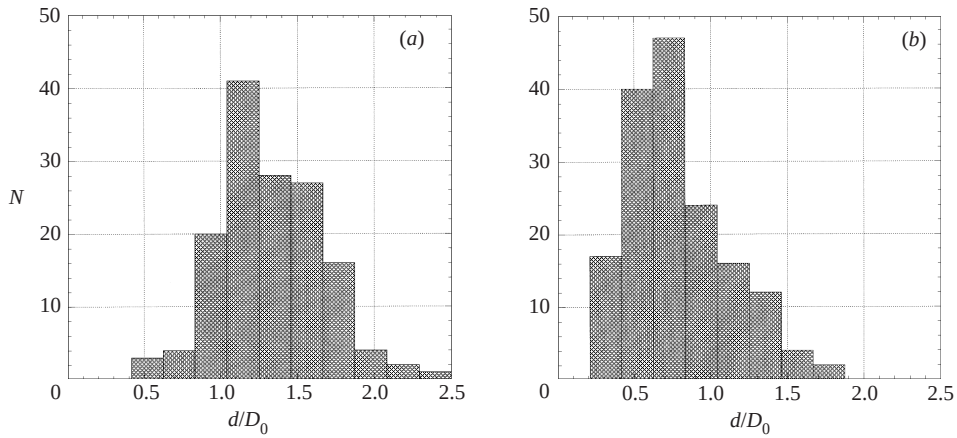

FIGURE 16. Example of drop size distribution in the natural case: (*a*) $We = 390$, $d/D_0 \simeq 1.33$ and $SD \simeq 0.33$; (*b*) $We = 1190$, $d/D_0 \simeq 0.79$ and $SD \simeq 0.32$.

cases, the drop diameter is of the order of D_0 and for all $\tilde{r}_0$ the diameters obtained with $We = 362$ are larger than with $We = 1190$.

3.6. *Drop formation and size*

The diameter of the drops in the natural case (without forcing) is not as well defined as in the forced case. A typical drop size distribution is presented in figure 16 for a water jet of diameter $D_0 = 2.7\,\text{mm}$ impacting on $D_i = 10.8\,\text{mm}$. The statistics

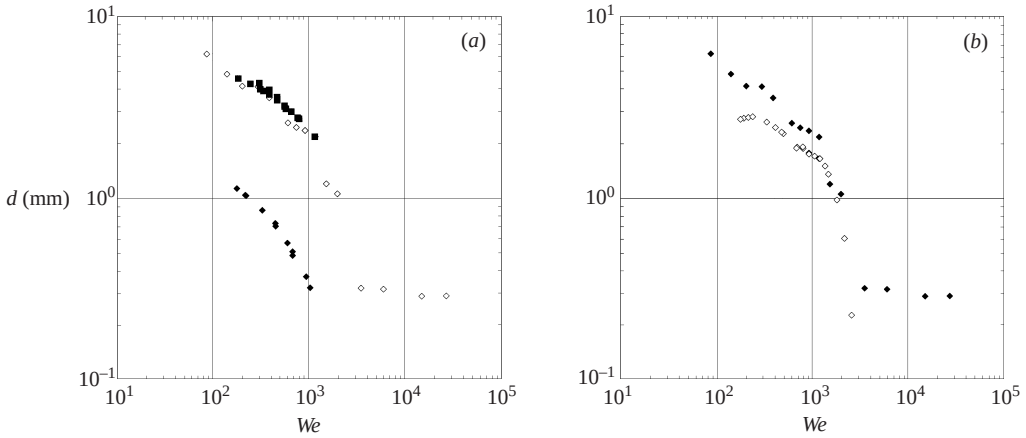

FIGURE 17. Evolution of the drop diameter d with the Weber number We: (a) ◆, water, $D_0 = 0.8$ mm, $D_i = 3.8$ mm; ◇, water, $D_0 = 2.7$ mm, $D_i = 10.8$ mm; ■, water, $D_0 = 5$ mm, $D_i = 20.8$ mm. (b) ◆, water, $D_0 = 2.7$ mm, $D_i = 10.8$ mm, ◇, ethanol, $D_0 = 2.7$ mm, $D_i = 10.8$ mm.

presented on figure 16 are based on a number, $N \approx 150$, of drop size measurements $d(i)$. From these distributions we define the mean diameter $d \equiv (1/N)\sum_{i=1}^{i=N} d(i)$, that corresponds to the statistical definition of D_{10} (Lefebvre 1989) and a standard deviation $SD \equiv \sqrt{\sum_{i=1}^{i=N}(d_i - d)^2/(N-1)}$. For the two cases presented in figure 16, we obtain $d/D_0 = 1.33 \pm 33\%$ for $We = 390$ and $d/D_0 = 0.79 \pm 32\%$ for $We = 1190$. This standard deviation is of the same order as that reported by Pandit & Davidson (1990) in the case of drops detaching from a rim in a bursting soap bubble.

The evolution of the mean drop diameter d with the Weber number is reported in figure 17. The effect of the injection diameter D_0 is presented in figure 17(a) and the effect of surface tension in figure 17(b). The main feature of the evolution is that the mean drop diameter decreases with the Weber number, first slowly for $We < 1200$ and more strongly for higher values of the Weber number. Above a certain value that corresponds to the point where the liquid sheet becomes turbulent, the drop size seems to reach a limit. According to figure 17(a), in the smooth regime, the mean drop diameter for a given Weber number is larger with $D_0 = 2.7$ mm than with $D_0 = 0.8$ mm. This suggests that the mean drop diameter is an increasing function of the jet diameter. However one also observes in figure 17(a) that the mean drop diameters obtained with $D_0 = 2.7$ mm and $D_0 = 5.0$ mm are almost the same. The increasing function thus seems to saturate for jet diameters larger than a few millimetres.

Finally, figure 17(b) shows that for a given Weber number, the mean drop diameter increases with surface tension.

4. Models

The flow is studied using the nomenclature presented in figure 18: r and z respectively stand for the radial and vertical axes, the origin of the coordinate system being the impact point of the jet. We denote $u(r, z)$ and $w(r, z)$ the corresponding velocity components, and $h(r)$ the film thickness at the location r.

4.1. *Characteristics of the flow at the edge of the impactor*

When a vertical liquid jet of diameter D_0 impacts with velocity U_0 a horizontal disc of diameter D_i, it spreads radially and its mean velocity and thickness are affected

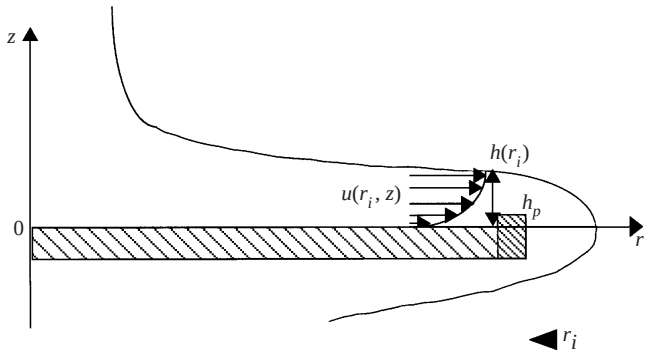

FIGURE 18. Diagram of the structure of the flow at the edge of the disc.

by the growth of the boundary layer on the impactor as presented in figure 18. A complete analysis of the radial spread of a liquid jet over a horizontal plane has been performed by Watson (1964). For a disc without a lip, Clanet (2001) shows that for diameter ratios $X \equiv D_i/D_0 \leqslant 0.366Re^{1/3}$, the effect of the disc is to alter the initial momentum flux as follows

$$\frac{I_e}{I_{max}} \approx 1 - \frac{1.02}{\sqrt{Re}} \left(\frac{D_i}{D_0}\right)^{3/2}, \tag{4.1}$$

where $Re = U_0 D_0/\nu$ is the Reynolds number and $I_e \equiv 2\pi\rho r_i \int_0^{h(r_i)} u(r_i, z)^2 \, \mathrm{d}z$ with $I_{max} = \pi\rho U_0^2 D_0^2/4$.

The characteristics of the liquid film, velocity U_e, and thickness h_e at the edge of the impactor are then deduced from the conservation of mass and momentum flux:

$$\pi D_i h_e U_e = \frac{\pi}{4} D_0^2 U_0, \tag{4.2}$$

and

$$\pi\rho D_i h_e U_e^2 = I_e, \tag{4.3}$$

so that

$$\frac{U_e}{U_0} = \frac{I_e}{I_{max}}, \quad \frac{h_e}{D_0} = \frac{D_0}{4D_i} \frac{I_{max}}{I_e}. \tag{4.4}$$

Since $I_e/I_{max} < 1$, the velocity in the film is reduced and the thickness increased. U_e and h_e are also affected by the lip at the edge of the impactor. To quantify this effect, we have performed direct flow measurements in the sheet.

4.2. *Characteristics of the flow in the sheet*

The velocity in the sheet is determined with a high-speed video camera, following the trajectory of ash dropped on the sheet surface. Two examples of such trajectories are presented in figure 19: time increases from top to bottom with a constant time step Δt. In the first image an ash particle, which appears as a small dark spot on the sheet, has been dropped at the location indicated by the arrow. After an initial acceleration phase which extends roughly from the first to the second image, the particle is convected towards the periphery with a constant velocity $U_e = 2.7\,\mathrm{m\,s^{-1}}$ in figure 19(*a*) and $U_e = 3.6\,\mathrm{m\,s^{-1}}$ in figure 19(*b*). The ratio of these velocities with the corresponding values of $U_0 = 3.09\,\mathrm{m\,s^{-1}}$ and $U_0 = 3.93\,\mathrm{m\,s^{-1}}$ are 0.87 and 0.91

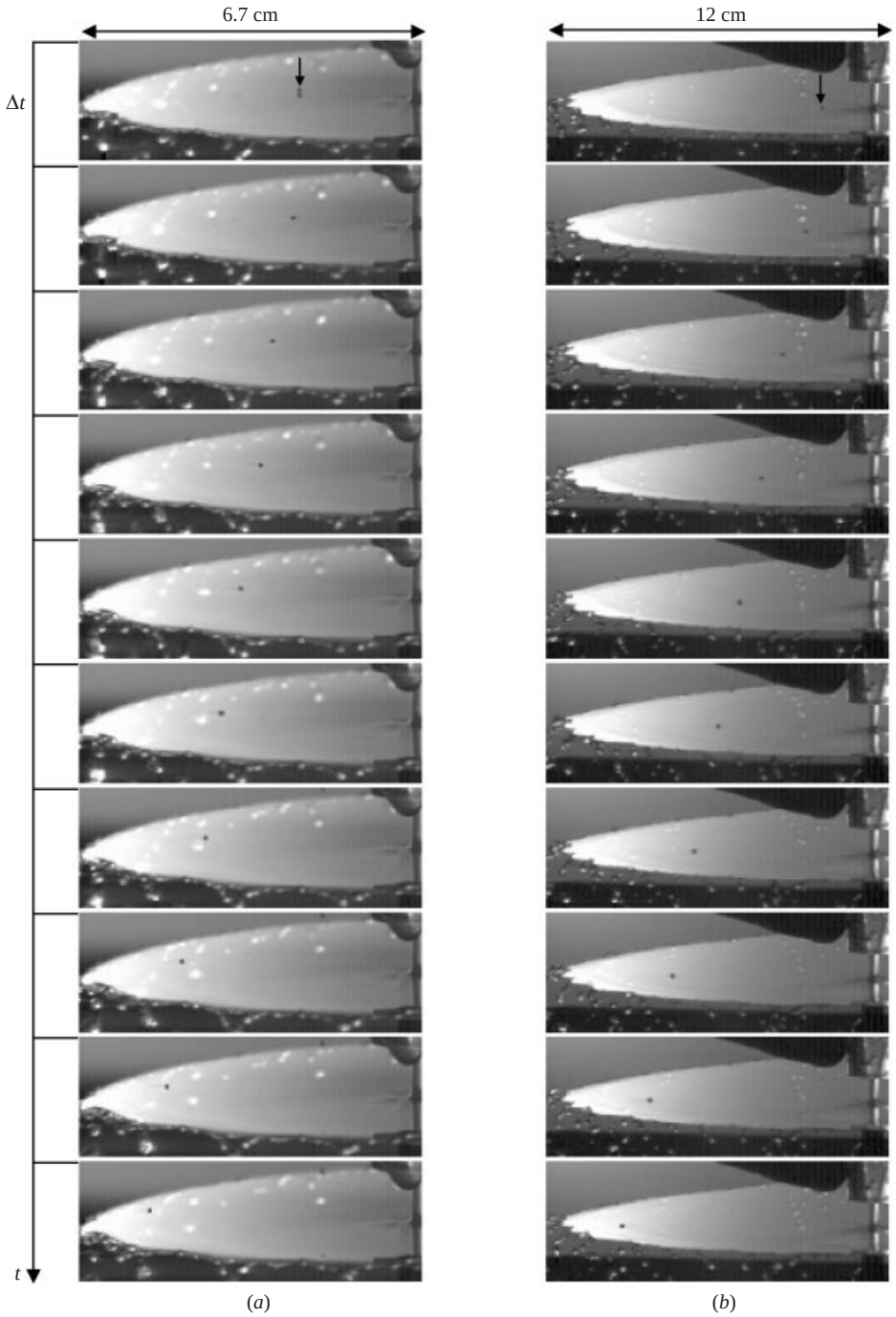

FIGURE 19. Trajectories of ash dropped on water liquid sheets obtained with $D_0 = 3\,\text{mm}$ and $D_i = 7\,\text{mm}$: (*a*) $U_0 = 3.09\,\text{m s}^{-1}$ and $\Delta t = 1.33\,\text{m s}^{-1}$; (*b*) $U_0 = 3.93\,\text{m s}^{-1}$ and $\Delta t = 2.22\,\text{m s}^{-1}$.

respectively. As expected from the presence of the lip, these values are slightly smaller than those predicted by equation (4.4).

The variation of the thickness $h(r)$ is measured with the interferometry set-up presented in figure 20(*a*): a cylindrical laser beam of wavelength $\lambda = 532\,\text{nm}$ is

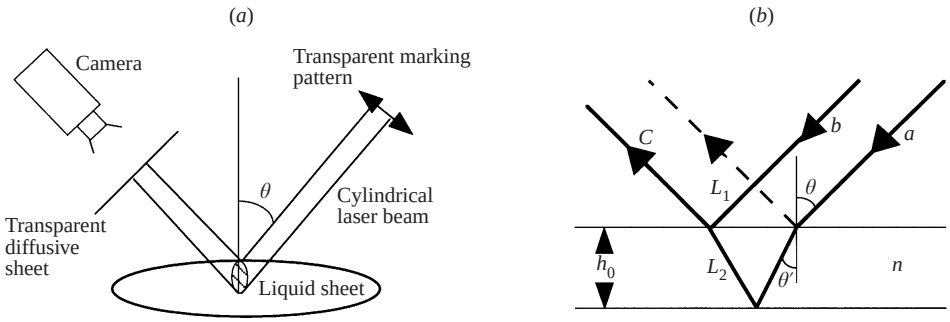

FIGURE 20. Interferometry technique used to measure the evolution of the film thickness: (*a*) general view of the set up, (*b*) interferometry principle.

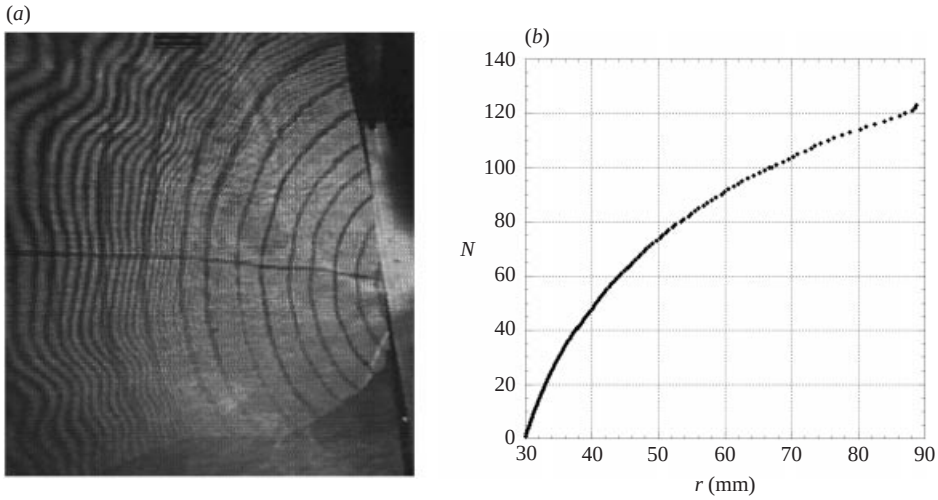

FIGURE 21. Interferometry pattern obtained with a liquid sheet of water ($We = 600$, $D_0 = 3\,\text{mm}$ and $R \simeq 90\,\text{mm}$): (*a*) interferometry pattern, (*b*) evolution of the number of fringes N with the distance from the impact r.

marked with equidistant circles centred on the impact point of the jet, using a transparent pattern. This marked beam is partly reflected by the upper surface of the liquid sheet (beam b) and partly refracted towards the lower surface (beam a) as presented in figure 20(*b*). The two beams interfere to give $c = a + b$ with the difference in their paths $\delta = 2nL_2 - L_1$, where $n = 1.33$ is the refraction index of water. Using the Snell–Descartes law $n \sin\theta' = \sin\theta$, this path difference reduces to $\delta = 2nh_0 \cos\theta'$, which implies that the distance between two bright fringes will correspond to a thickness variation:

$$\Delta h_0 = \frac{\lambda}{2n \cos\theta'}. \tag{4.5}$$

In our experiments, the angle θ between the laser beam and the liquid sheet was maintained constant and equal to $\theta = 27^\circ$ so that $\theta' = 20^\circ$. From equation (4.5), this corresponds to a thickness variation $\Delta h_0 \simeq 0.21\,\mu\text{m}$ between two fringes. An example of the interferometry pattern obtained with water ($We = 600$, $D_0 = 3\,\text{mm}$ and $R \simeq 90\,\text{mm}$) is presented in figure 21(*a*), where the distance between the marked circles is 5 mm.

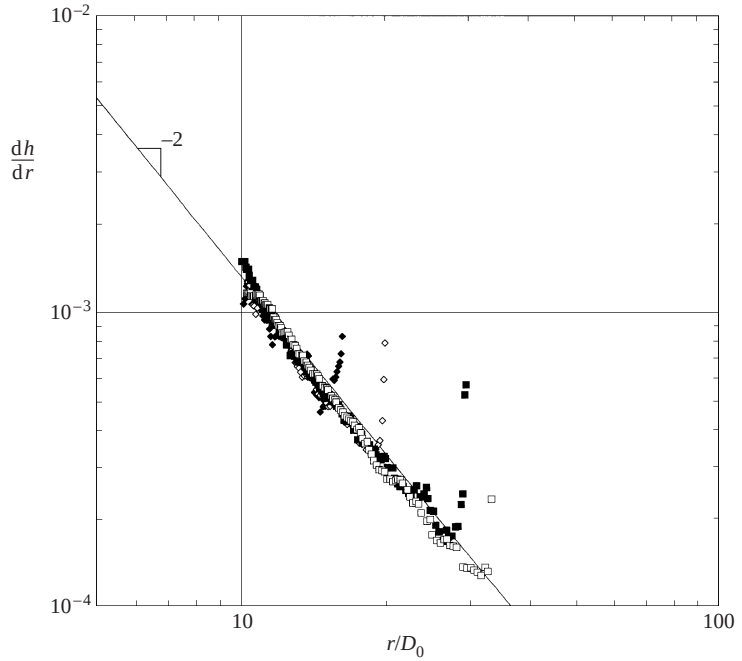

FIGURE 22. Variation of the film thickness dh/dr as a function of the radial distance r/D_0, observed with water, $D_0 = 3\,\text{mm}$, $D_i = 7\,\text{mm}$: ◆, $R = 50\,\text{mm}$, $We = 320$; ◇, $R = 60\,\text{mm}$, $We = 400$; ■, $R = 90\,\text{mm}$, $We = 600$; □, $R = 110\,\text{mm}$, $We = 730$.

From these images, we extract the evolution of the number of fringes $N(r)$ with the distance from the impact r. The evolution corresponding to figure 21(a) is presented in figure 21(b). The evolution starts at an arbitrary radius r_0 that corresponds to the first visible fringe. From this radius up to the maximal radial extension R, we obtain the variation of thickness between r and r_0, using the relation $h(r) - h(r_0) = N(r)\ \Delta h_0$, or $dh/dr = \Delta h_0 dN/dr$. The variation of the thickness dh/dr observed for a water sheet, $D_0 = 3\,\text{mm}$, $D_i = 7\,\text{mm}$, is presented in figure 22, for different Weber numbers ranging from 320 to 730. The striking feature of figure 22 is that dh/dr is mainly a function of r/D_0 with a -2 power law dependence, $dh/dr \approx 0.133(r/D_0)^{-2}$. This implies that $h(r)/D_0 \approx 0.133 D_0/r + C$, where C is a constant. C can be determined through the conservation of mass, which relates $h(r)$ and $U(r)$:

$$\frac{h(r)}{D_0}\frac{U(r)}{U_0} = \frac{1}{8}\frac{D_0}{r}. \tag{4.6}$$

Since $U(r)/U_0$ does not depend on r, equation (4.6) implies that $h(r)/D_0 = [\frac{1}{8}U_0/U_e]D_0/r$, so that C is effectively nil. Moreover, if $U_e/U_0 \approx 0.9$, one expects that $h(r)/D_0 = 0.138 D_0/r$, which is close to the value reported in figure 22.

If we neglect the friction with the surrounding air, the conservation of the momentum flux at any radial location is written

$$\frac{h(r)}{D_0}\left(\frac{U(r)}{U_0}\right)^2 = \frac{1}{8}\frac{D_0}{r}\frac{I_e}{I_{max}}. \tag{4.7}$$

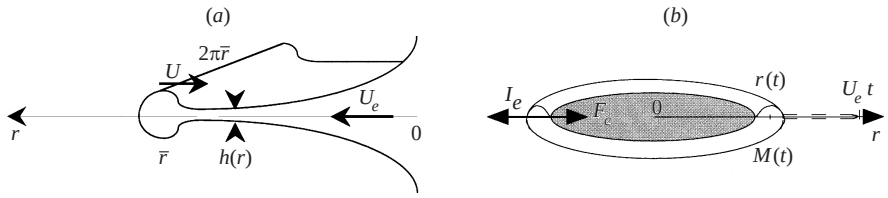

FIGURE 23. (*a*) Diagram for the dynamics of the rim. (*b*) Presentation of the formation problem.

Together, with equation (4.6), the characteristics of the flow in the sheet are obtained as

$$\frac{U}{U_0} = \frac{I_e}{I_{max}}, \quad \frac{h(r)}{D_0} = \frac{1}{8}\frac{D_0}{r}\frac{I_{max}}{I_e}. \tag{4.8}$$

4.3. *Evolution of the liquid sheet radius, R*

The argument developed by Taylor (1959*c*) for a constant thickness sheet with no initial velocity can be extended to sheets with variable thickness and fed with a constant velocity U_e, as presented in figure 23(*a*). For the dynamics of the rim, characterized by its mass $M(t)$ and velocity $U(t)$, one obtains for the mass and momentum evolution

$$\frac{\mathrm{d}M}{\mathrm{d}t} = 2\pi\rho r h(r)(U_e - U), \tag{4.9}$$

and

$$\frac{\mathrm{d}(MU)}{\mathrm{d}t} = -4\pi\sigma r + \frac{\mathrm{d}M}{\mathrm{d}t}U_e, \tag{4.10}$$

There should be an additional curvature term in equation (4.10) resulting from the curvature of the rim centreline. This term is of order r_{rim}/r, where r_{rim} is the radius of the rim. In our applications, this term is much smaller than $4\pi r\sigma$ and is neglected in the following discussion. The set of equations (4.9) and (4.10) is Galilean invariant: if U is changed to $U' + K$ where K is a contant, the equations for M and U' are the same as for M and U. The velocity U_e is simply changed to $U_e - K$. If we look for stationary solutions in the frame of the laboratory, $U = 0$, equations (4.9) and (4.10) imply that the only position where the sheet can remain at rest corresponds to the location $\bar{r}$, where $h(\bar{r}) = 2\sigma/(\rho U_e^2)$. To examine the stability of this equilibrium, we perturb the rim location, $r = \bar{r} + \delta r$, and follow the evolution of its velocity, δU. The linearization of equations (4.9) and (4.10) leads to

$$\frac{\delta U}{\delta r} = \frac{\rho U_e^3}{4\sigma}\left(\frac{\mathrm{d}h}{\mathrm{d}r}\right)_{\bar{r}}. \tag{4.11}$$

The equilibrium is thus stable if $(\mathrm{d}h/\mathrm{d}r)_{\bar{r}} < 0$ and unstable if the film thickness increases with the distance. In our case, the film thickness decreases as $1/r$, so that the equilibrium is stable. In this model, there is no mass shedding and the rim increases in mass without breaking. Regarding its relevance to the stationary liquid sheet, one observes that the model can only be valid on time scales shorter than the time required for the rim to destabilize and break. On a longer time scale, we have to take into account drop shedding. We respectively denote $\mathrm{d}m_d/\mathrm{d}t$ and v_d the mass of liquid emitted per unit of time and the mean drop velocity. Equations (4.9) and (4.10)

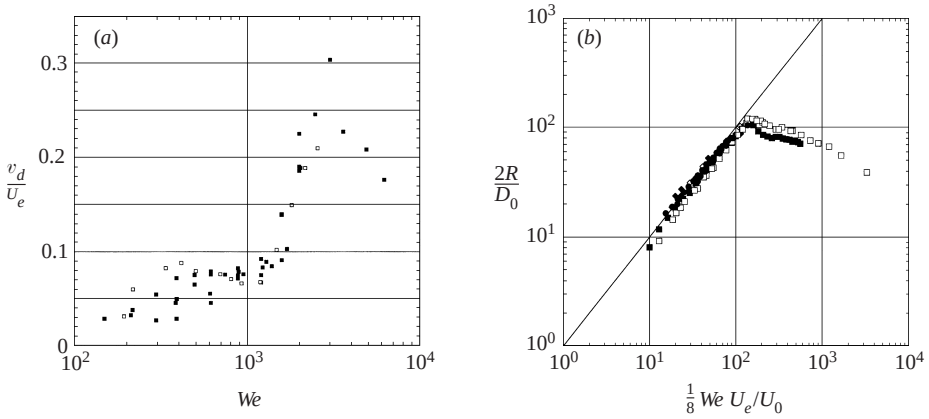

FIGURE 24. (*a*) Evaluation of the relative drop velocity as a function of the Weber number. (*b*) Comparison between the non-dimensional experimental sheet diameter $2R/D_0$ and equation (4.16) in the limit $v_d/U_e \ll 1$: ◆, $D_0 = 0.8$ mm, $D_i = 3.8$ mm and water; ◇, $D_0 = 0.8$ mm, $D_i = 3.8$ mm and ethanol; ■, $D_0 = 2.7$ mm, $D_i = 10.8$ mm and water; □, $D_0 = 2.7$ mm, $D_i = 10.8$ mm and ethanol; ●, $D_0 = 5$ mm, $D_i = 20.8$ mm and water; – – –, equation (4.16).

become

$$\frac{\mathrm{d}M}{\mathrm{d}t} = 2\pi\rho r h(r)(U_e - U) - \frac{\mathrm{d}m_d}{\mathrm{d}t} \tag{4.12}$$

and

$$\frac{\mathrm{d}MU}{\mathrm{d}t} = -4\pi\sigma r + \frac{\mathrm{d}M}{\mathrm{d}t}U_e - \frac{\mathrm{d}m_d}{\mathrm{d}t}v_d. \tag{4.13}$$

An interesting limit for our study is to consider this new system on a long time scale, where the rim has a constant mass and fixed location. In this limit, $\mathrm{d}m_d/\mathrm{d}t$ is equal to the mass flow rate, $Q \equiv \pi\rho D_0^2 U_0/4$, and equations (4.12) and (4.13) reduce to

$$\frac{Q}{2\pi r} = \rho h(r) U_e \tag{4.14}$$

and

$$\frac{Q}{2\pi r} = \frac{2\sigma}{U_e - v_d}. \tag{4.15}$$

These equations show that the equilibrium occurs at the location where $h(r) = [2\sigma/(\rho U_e^2)]/(1 - v_d/U_e)$. Since $rh(r) = (U_0/U_e)D_0^2/8$ (see equation (4.7)), we deduce that the maximal radial extension R is given by

$$\frac{2R}{D_0} = \frac{We}{8}\frac{U_e}{U_0}\left(1 - \frac{v_d}{U_e}\right). \tag{4.16}$$

In the limit $v_d/U_e \ll 1$ and $U_e/U_0 = 1$, we recover Taylor's result. The experimental measurements of the ratio v_d/U_e are presented in figure 24(*a*) as a function of the Weber number. For larger Weber number, $We \approx 3000$, this ratio can reach 0.25. In the smooth range of interest this ratio is of the order of 0.05 and never exceeds 0.1. We thus neglect the effect of the ejected drops and present in figure 24(*b*), the non-dimensional experimental sheet diameter, $2R/D_0$, versus the ratio $(We/8)(U_e/U_0)$.

This comparison reveals a good agreement between the experimental data and equation (4.16), up to $(We/8)(U_e/U_0) \simeq 110$, that is $We \approx 1000$. Above this value, the effect of v_d/U_e and of the surrounding air can no longer be neglected.

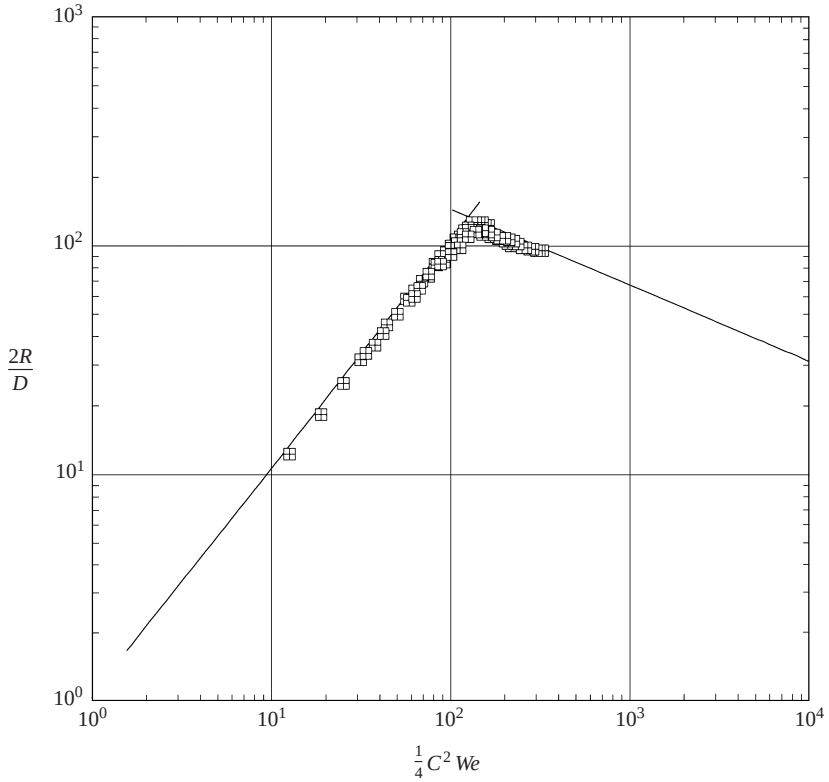

FIGURE 25. Presentation of Savart's experimental results (⊞), together with Huang's data (——).

Results of Savart and Huang, already discussed by Taylor (1959*a–c*), are presented in figure 25. Note that these authors considered the liquid sheet resulting from the impact of two facing jets coming out of two thin wall holes of diameter D. The main differences with our configuration are that:

viscous losses are negligible since there is no impactor;

at the same velocity, the flow rate is doubled due to the two facing jets;

the type of injectors used by Savart and Huang introduce a contraction of the jet that implies that the jet diameter D_0 is related to the geometrical diameter D through the relation $D_0 = CD$, where $C \simeq 0.79$.

The same approach as used to obtain equation (4.16) leads here to the relation

$$\frac{2R}{D} = \frac{2C^2}{8}\frac{\rho U_0^2 D}{\sigma}\left(1 - \frac{v_d}{U_e}\right), \tag{4.17}$$

where the factor 2 accounts for the two jets and the factor C^2 for the contraction of the jet. Savart's experimental results are shown in figure 25, where the scaled sheet radius $2R/D$ is plotted versus $C^2We/4$. We have also drawn as a continuous line the experimental law given by Huang (1970): $2R/D \approx 0.167We$ for $We < 1000$ and $2R/D \approx 1250We^{-1/3}$ for $We > 1000$. The first point to note is the consistency of both sets of data. The second is the one to one correpondance with the value extracted from equation (4.17). This linearity holds up to $C^2We/4$, that is up to a Weber number of the order of 830.

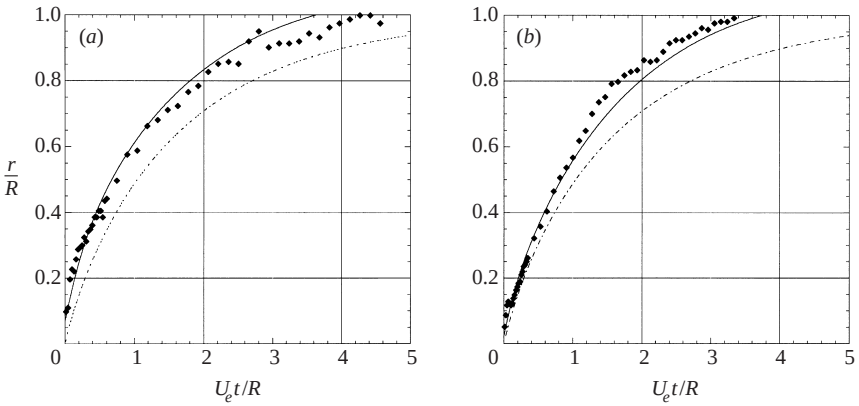

FIGURE 26. Comparison between the experimental trajectories obtained with water, $D_0 = 3\,\text{mm}$, $D_i = 7\,\text{mm}$ and the numerical integration of (4.19) and (4.20). The symbols are the experimental points, the continuous line is the numerical integration and the dotted line represents the approximate solution described by equation (4.21). (*a*) $We = 138$, (*b*) $We = 375$.

4.4. *Dynamics of the liquid sheet formation and destruction*

4.4.1. *Liquid sheet formation*

We define t_{birth} as the instant when the liquid jet first touches the impactor and $t_{stationary}$ the time at which the stationary regime is first achieved. To study the dynamics of formation we need to determine the edge trajectory $r(t)$, from t_{birth} to $t_{stationary}$. An example of such dynamics is presented in figure 10. This problem is discussed with the notation presented in figure 23(*b*), where the liquid sheet is grey and the rim characterized by its radial location $r(t)$ and its mass $M(t)$. If the rim had followed the flow, its location would be $U_e t$, where $t = 0$ is defined to be t_{birth}. Assuming that the liquid remains in the rim and is not lost via drops during the formation process, which is reasonable according to figure 10, the mass conservation is written:

$$M(t) = M_0 + 2\pi \int_{r(t)}^{U_e t} rh(r)\,\mathrm{d}r = M_0 + \frac{\pi}{4}\rho D_0^2 \frac{U_0}{U_e}(U_e t - r), \tag{4.18}$$

where M_0 is the initial mass of the rim, of the order of $\pi/4\rho D_0^3$. The dynamics of the rim results from the competition between the pushing momentum flux I_e and the pulling capillary force F_c, so that the momentum evolution is again described by equation (4.10). Using R and U_e as the characteristic length and velocity, the non-dimensional form of the above system is

$$\tilde{M} = \tilde{M}_0 + \tilde{t} - \tilde{r}, \tag{4.19}$$

where all the dimensionless quantities are indicated with a tilde. Also,

$$\frac{\mathrm{d}}{\mathrm{d}\tilde{t}}[\tilde{M}(1 - \dot{\tilde{r}})] = \tilde{r}, \tag{4.20}$$

where the dot stands for time derivative. This system has to be solved with the initial conditions $\tilde{r}(0) = 0$, $\dot{\tilde{r}}(0) = 1$ and $\tilde{M}(0) = (D_0/R)U_e/U_0$. The numerical integration of the system (4.19) and (4.20) is compared to the experimental trajectories in figure 26 for different Weber numbers. The trajectory corresponding to figure 10 is presented in figure 26(*b*). Both comparisons reveal a satisfactory agreement between the experimental trajectory and the numerical integration of the system of equations

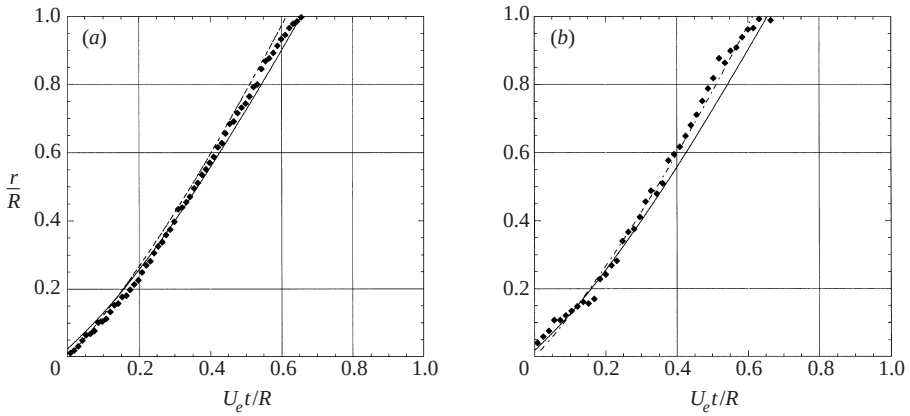

FIGURE 27. Comparison between the experimental trajectories obtained with water, $D_0 = 3$ mm, $D_i = 7$ mm and the numerical integration of (4.22) and (4.23). The symbols stand for the experimental points, the continuous line for the numerical integration and the dotted line for the quasi-steady approximation. (*a*) $We = 375$, (*b*) $We = 492$.

(4.19) and (4.20). The nonlinear evolution of the edge location noted in § 3.4.1 is demonstrated and we obtain from figure 26 that $\tilde{t}_{stationary} \approx 4$ whereas the time it takes to reach $\tilde{r} = 1/2$ is roughly 0.8.

There is an approximate analytical solution of the above system of equations: the left-hand side of (4.20) can be decomposed in two terms $(1-\dot{\tilde{r}})^2 - \tilde{M}\ddot{\tilde{r}}$. The first one represents the momentum variation due to the entrainment of new fluid. The second is the classical mass times acceleration product. Assuming that most of the momentum variation is related to the entrainment, equation (4.20) reduces to $\dot{\tilde{r}} = 1 - \sqrt{\tilde{r}}$ which can be integrated as

$$\sqrt{\tilde{r}} + \ln(1 - \sqrt{\tilde{r}}) = -\tilde{t}/2. \tag{4.21}$$

This implicit trajectory $\tilde{r}(\tilde{t})$ is the dotted line in figure 26. The difference with the measured trajectory indicates that the effect of the acceleration cannot be neglected. Note that equation (4.21) also describes the trajectory of antisymmetrical waves propagating inwards.

4.4.2. *Liquid sheet destruction*

An example of sheet destruction is presented in figure 11, and one observes that once the liquid jet is cut, the liquid sheet remains undisturbed until the free end of the jet touches the impactor and creates a hole, the size of which increases up to the edge of the stationary sheet. We define t_{cut} as the instant when the free edge of the jet touches the impactor and t_{death} the time when the hole reaches the edge of the stationary liquid sheet. To study liquid sheet destruction we need to determine the dynamics of the hole from t_{cut} to t_{death}.

Compared to the formation problem, the only difference is that the two forces acting on the rim of the hole, I_e and F_c, now act in the same direction. The corresponding system, non-dimensionalized with R and U_e, is

$$\tilde{M} = \tilde{M}_0 + \tilde{r} - \tilde{t} \tag{4.22}$$

and

$$\frac{\mathrm{d}}{\mathrm{d}\tilde{t}}[\tilde{M}(\dot{\tilde{r}} - 1)] = \tilde{r}. \tag{4.23}$$

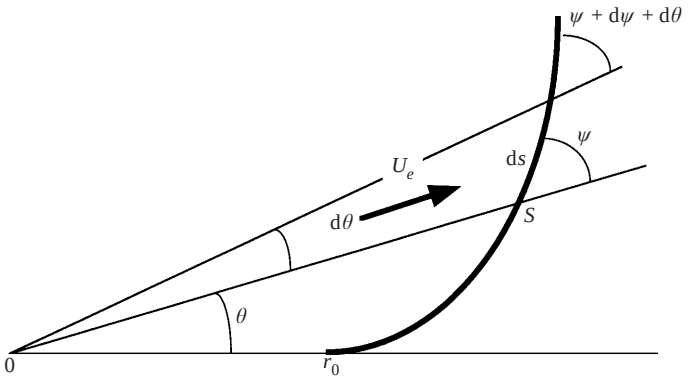

FIGURE 28. Presentation of the polar coordinate system used to establish the cusp shape equations system.

Equations (4.22) and (4.23) are respectively equivalent to equations (4.19) and (4.20). They have to be integrated with the initial conditions, $\tilde{r}(0) = 0$, $\dot{\tilde{r}}(0) = 1$ and $\tilde{M}(0) = (D_0/R)U_e/U_0$. The numerical integration of (4.22) and (4.23) is compared to the experimental trajectories in figure 27, for two different Weber numbers. The trajectory presented in figure 27(*a*) corresponds to the sequence presented in figure 11. Both comparisons reveal a good agreement between the experimental trajectory and the integration of our model. The quasi-linear evolution with time of the edge location observed in § 3.4.2 is verified. The characteristic time of destruction of the sheet is $\tilde{t}_{death} \approx 0.65$ and the halfway distance $\tilde{r} = 1/2$ is reached at $\tilde{t} \approx 0.35$.

The approximate solution obtained, as in the previous section, by neglecting the acceleration term in the momentum variation is here

$$\sqrt{\tilde{r}} - \ln(1 + \sqrt{\tilde{r}}) = \tilde{t}/2. \tag{4.24}$$

Due to the quasi-linearity of the observed trajectory, this approximate solution is a good description of the phenomenon. Again equation (4.24) also describes the trajectory of antisymmetrical waves propagating outwards.

4.5. *Shape of the cusps observed at the periphery of the sheet*

This section is devoted to the study of the forced cusps presented in figures 13 and 14. The questions addressed concern their shape and the dynamics of the liquid inside. As a first step, we follow Taylor's (1959*c*) analysis to establish the set of equations describing the shape of the cusps using the polar coordinate system presented in figure 28. The apex is defined by $\theta = 0$ and $r = r_0$, $U_c(s)$ is the velocity of the fluid inside the cusp at the curvilinear location s from the apex, and $S_c(s)$ the cross-section of the cusp. In a stationary regime, the mass conservation in the cusp takes the form

$$\frac{\mathrm{d}(U_c S_c)}{\mathrm{d}\theta} = \tfrac{1}{8} D_0^2 U_0. \tag{4.25}$$

To obtain equation (4.25), we have used the mass conservation in the liquid sheet with $u(r) = U_e$ and the geometrical relation $\sin\psi = r\,\mathrm{d}\theta/\mathrm{d}s$. Using the same relations, the momentum conservation along the cusp is

$$\frac{\mathrm{d}(U_c^2 S_c)}{\mathrm{d}\theta} = \tfrac{1}{8} D_0^2 U_0 U_e \cos\psi. \tag{4.26}$$

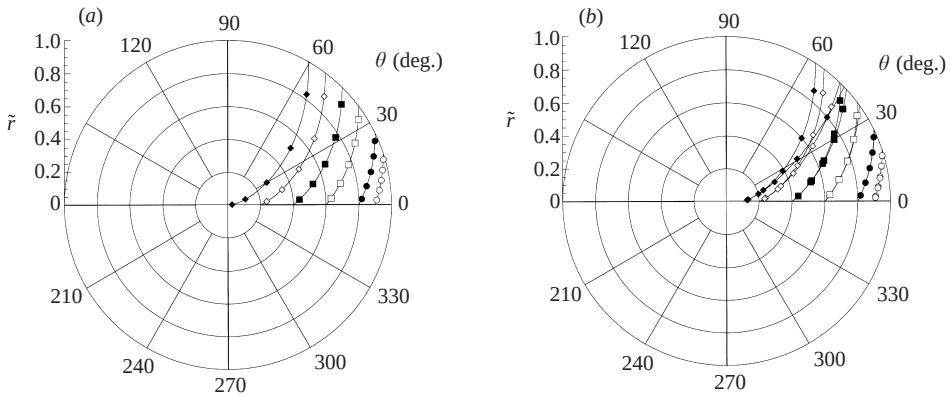

FIGURE 29. (*a*) Evolution of the shape of the cusp with the apex location, r_0: ◆, $\tilde{r}_0 = 0.1$; ◇, $\tilde{r}_0 = 0.2$; ■, $\tilde{r}_0 = 0.4$; □, $\tilde{r}_0 = 0.6$; ●, $\tilde{r}_0 = 0.8$; ○, $\tilde{r}_0 = 0.9$. (*b*) Comparison between the numerical integration of the shape and the approximate logarithmic spiral.

In the direction perpendicular to the cusp, the momentum conservation takes the form

$$U_c^2 S_c \sin\psi \left(1 + \frac{\mathrm{d}\psi}{\mathrm{d}\theta}\right) = \frac{2\sigma}{\rho} r - \tfrac{1}{8} D_0^2 U_0 U_e \sin^2\psi. \tag{4.27}$$

In this expression for momentum conservation, we have neglected the surface tension effect related to the curvature of the cusp. Compared to the free edge effect $2\sigma\,\mathrm{d}s$, the curvature effect is of the order $1/We^2$ and our study was conducted for $We \gg 1$. Scaling with U_e and $R = (We/16)D_0(U_e/U_0)$, the set of equations (4.25), (4.26) and (4.27), respectively become

$$\tilde{U}_c \tilde{S}_c = \frac{1}{8}\left(\frac{D_0}{R}\right)^2 \left(\frac{U_0}{U_e}\right)\theta, \tag{4.28}$$

$$\frac{\mathrm{d}(\theta \tilde{U}_c)}{\mathrm{d}\theta} = \cos\psi, \tag{4.29}$$

$$\theta \tilde{U}_c \sin\psi \left(1 + \frac{d\psi}{d\theta}\right) = \tilde{r} - \sin^2\psi, \tag{4.30}$$

where the tilde denotes non-dimensionalized quantities. The mass conservation (4.28) results from the integration of equation (4.25), with the initial condition $S = 0$ at the apex $r = r_0, \theta = 0$.†

The above set of equations must be solved with the initial conditions: at $\theta = 0$, $\tilde{r} = \tilde{r}_0$, $\psi = \arcsin\sqrt{\tilde{r}_0}$, $\tilde{U}_c = \sqrt{1 - \tilde{r}_0}$. The unknowns are $\tilde{S}_c(\theta)$, $\tilde{U}_c(\theta)$ and $\tilde{r}(\theta)$. The angle ψ is not an additional unknown since it is related to $\tilde{r}$ through the geometrical relation $1/\sin^2\psi = 1 + ((1/\tilde{r})(\mathrm{d}\tilde{r}/\mathrm{d}\theta))^2$. The cross-section of the cusp is obtained through equation (4.28), whereas the cusp shape $\tilde{r}(\theta)$ and its velocity $\tilde{U}_c(\theta)$ are described by the two autonomous equations (4.29) and (4.30). From this, one deduces that the cusp shape must be a function only of the apex location $\tilde{r}_0$: $\tilde{r}(\theta) = \mathscr{F}(\tilde{r}_0)$.

† A more accurate assumption would be to take the section at the obstacle to be of order of the local sheet thickness. This correction term is of order $(\pi/32)(D_0/r_0)^2(U_0/U_e)(1/\theta)$. Since $r > D_i$ and $D_0/D_i \approx 0.25$, this correction is only sensitive in the first angle degree and vanishes for angles larger than 1°. To simplify the discussion, without loss of generality, the condition $S = 0$ at the apex is more appropriate.

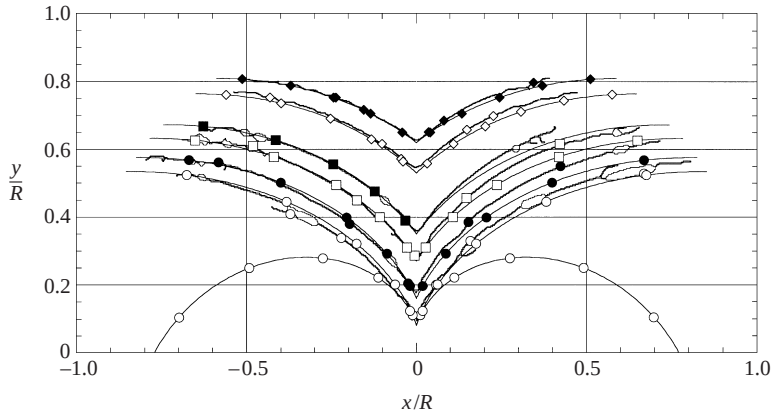

FIGURE 30. Comparison between the measured cusp shape with $We = 585$, $R = 8$ cm, $Re = 10\,700$ (lines) and the theoretical shape: ◆, $\tilde{r}_0 = 0.62$; ◇, $\tilde{r}_0 = 0.53$; ■, $\tilde{r}_0 = 0.35$; □, $\tilde{r}_0 = 0.27$; ●, $\tilde{r}_0 = 0.16$; ○, $\tilde{r}_0 = 0.08$ and cardioid.

The evolution of the cusp shape with $\tilde{r}_0$ is presented in figure 29(a). The main feature is that the mean curvature of the cusp remains almost constant, of the order of 1, for all apex locations. We also observe that the cusp forms an angle with the circle at $\tilde{r} = 1$, contrary to the cardioid $\tilde{r} = \frac{1}{2}(1 + \sin(\theta - \theta_0))$ that characterizes the stationary waves on the expanding liquid sheet (Taylor 1959*b*).

When we force a cusp on the liquid sheet as presented in figure 13, little liquid is shed and it is reasonable to compare the experimental shapes presented in figure 14 to the theoretical cusp shape described by the above set of equations. This comparison is given in figure 30. The agreement between the measured profiles and the theoretical ones is reasonable. In the case $\tilde{r}_0 = 0.08$, we report the corresponding standing wave profile on figure 30 which clearly demonstrates that the cusp shape is not a cardioid.

Looking for an approximate theoretical expression for the shape $\tilde{r}(\theta)$, we make the assumption that ψ remains almost constant along the cusp. Using the geometrical equation $(1/r)(\mathrm{d}r/\mathrm{d}\theta) = 1/\tan\psi$, in the limit $\psi \simeq \psi_0 = \arcsin\sqrt{\tilde{r}_0}$, we obtain the logarithmic spiral

$$\tilde{r}(\theta) = \tilde{r}_0 \exp\left(\sqrt{\frac{1-\tilde{r}_0}{\tilde{r}_0}}\theta\right). \tag{4.31}$$

This approximate solution of the cusp shape is compared to the numerical integration in figure 29(b). This comparison reveals a good agreement between the logarithmic spiral and the numerically integrated shape in the range $\tilde{r}_0 \in [0.4, 1]$. For smaller values of $\tilde{r}_0$, the predicted radius is overestimated. This approximate form of the cusp can be used to evaluate its radius of curvature $\tilde{R}_c \equiv (\tilde{r}^2 + \tilde{r}_\theta^2)^{3/2}/(\tilde{r}^2 + 2\tilde{r}_\theta^2 - \tilde{r}\tilde{r}_{\theta\theta})$, where $\tilde{r}_\theta = \mathrm{d}\tilde{r}/\mathrm{d}\theta$ and $\tilde{r}_{\theta\theta} = \mathrm{d}^2\tilde{r}/\mathrm{d}\theta^2$. Using equation (4.31), the expression for the radius of curvature reduces to

$$\tilde{R}_c \approx \sqrt{\tilde{r}_0}\exp\left(\sqrt{\frac{1-\tilde{r}_0}{\tilde{r}_0}}\theta\right)$$

which tends to 1 in the limit $\tilde{r}_0 \approx 1$.

To obtain the transit time of the drops on the cusp and the centrifgal acceleration they support when travelling from the apex to the cusp extremity $\tilde{r} = 1$, we study numerically the evolution with $\tilde{r}_0$ of different cusp characteristics. Using the suffix

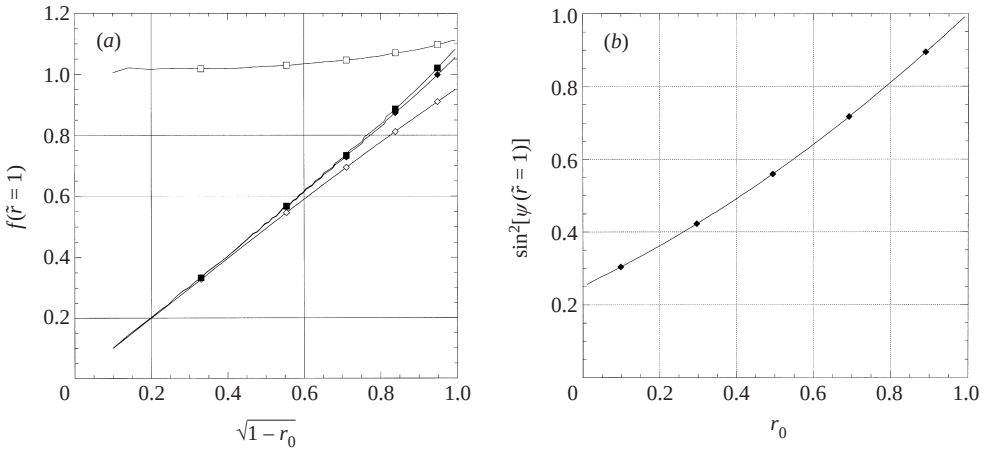

FIGURE 31. Evolution of the characteristics of the cusp at $\tilde{r}=1$: (*a*) as functions of $\sqrt{1-\tilde{r}_0}$: ◆, θ_{max}; ◇, $\tilde{U}_{max}$; ■, $\tilde{s}_{max}$; □, $\tilde{t}_{max}$; (*b*) $\sin^2\psi_{max}$.

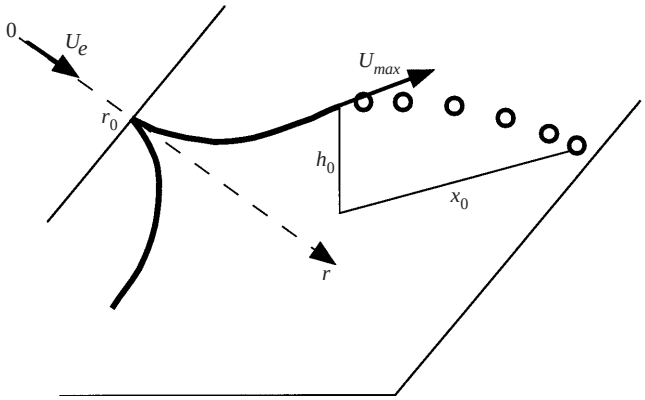

FIGURE 32. Experimental method used to determine the ejection velocity $\tilde{U}_{max}$.

max to designate quantities at the location where $\tilde{r}=1$, we present in figure 31(*a*), the evolutions of θ_{max}, $\tilde{U}_{max}$ and $\tilde{s}_{max}$. It appears that they all vary linearly with $\sqrt{1-\tilde{r}_0}$, with respective slopes 1.04, 0.96 and 1.05. These evolutions have the interesting consequence that the travel time $\tilde{t}_{max} \equiv \int_0^{s_{max}} \mathrm{d}\tilde{s}/\tilde{U}_c$ is almost independant of the apex location and remains equal to 1. The evolution of the ejection angle ψ_{max} is presented in figure 31(*b*) and reveals that $\sin^2\psi_{max}$ varies linearly with $\tilde{r}_0$ when $\tilde{r}_0 \simeq 1$.

To check the validity of the results obtained for the dynamics of the cusps we have measured the ejection velocity $\tilde{U}_{max}$ with the experimental set-up presented in figure 32, to make the comparison with the theoretical value:

$$\tilde{U}_{max} = 0.96\sqrt{1-\tilde{r}_0}. \tag{4.32}$$

The apex location $\tilde{r}_0$ was varied using a 100 μm tungsten wire and for each location we measured the distance x_0 travelled by the drop from the ejection point on the liquid sheet to a reception box. Knowing the distance h_0 from the sheet to the box,

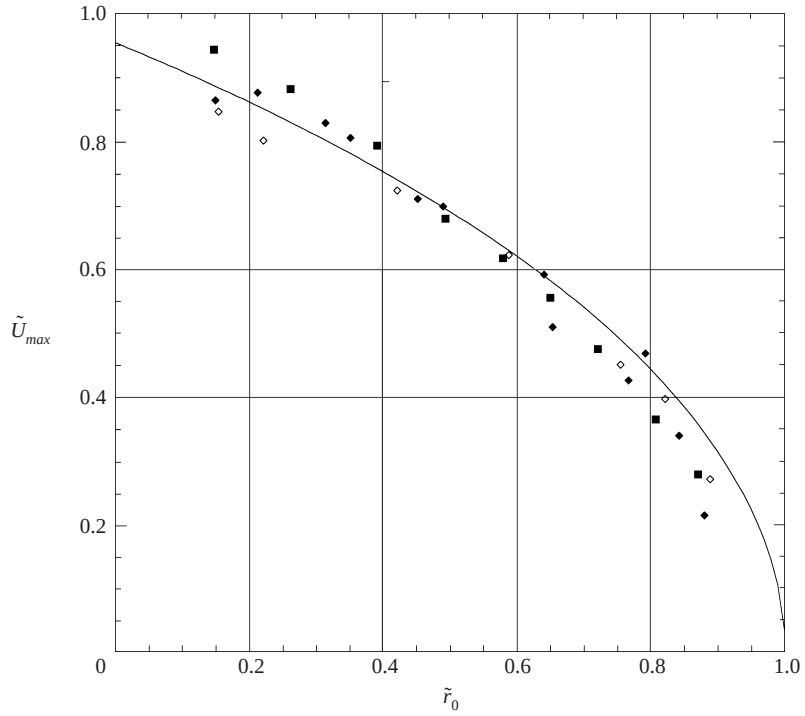

FIGURE 33. Comparison between the ejection velocity measured experimentally and the one calculated: ◆, $We = 454$; ◇, $We = 510$; ■, $We = 709$; ——, theoretical expression.

we deduce the ejection velocity, assuming a ballistic trajectory for the drops:

$$\tilde{U}_{max} = \sqrt{\frac{g x_0^2}{2 h_0 U_e^2}}. \tag{4.33}$$

The comparison between the measured ejection velocity obtained with this method and equation (4.32) is presented in figure 33. This comparison reveals a good correlation between the measurements and the theoretical predictions. The centrifugal acceleration $\tilde{\gamma}_c$ acting on the drops as they travel from the apex to the cusp extremity can thus be evaluated as

$$\tilde{\gamma}_c \equiv \tilde{U}_c^2 / \tilde{R}_c \approx \frac{1 - \tilde{r}_0}{\sqrt{\tilde{r}_0}} \exp\left(-\sqrt{\frac{1 - \tilde{r}_0}{\tilde{r}_0}} \theta \right).$$

In the limit $\tilde{r}_0 = 1 - \epsilon$, we find

$$\tilde{\gamma}_c \approx \epsilon. \tag{4.34}$$

For the evolution of the cusp section $\tilde{S}_{max}$ at $\tilde{r} = 1$, equation (4.28) leads to

$$\tilde{S}_{max} = \frac{1}{8} \left(\frac{D_0}{R} \right)^2 \left(\frac{U_0}{U_e} \right) \frac{\theta_{max}}{\tilde{U}_{max}}. \tag{4.35}$$

Using the expressions obtained for θ_{max} and $\tilde{U}_{max}$, the expression for the section simplifies and in dimensional form is

$$S_{max} = \frac{1}{8} \frac{U_0}{U_e} D_0^2. \tag{4.36}$$

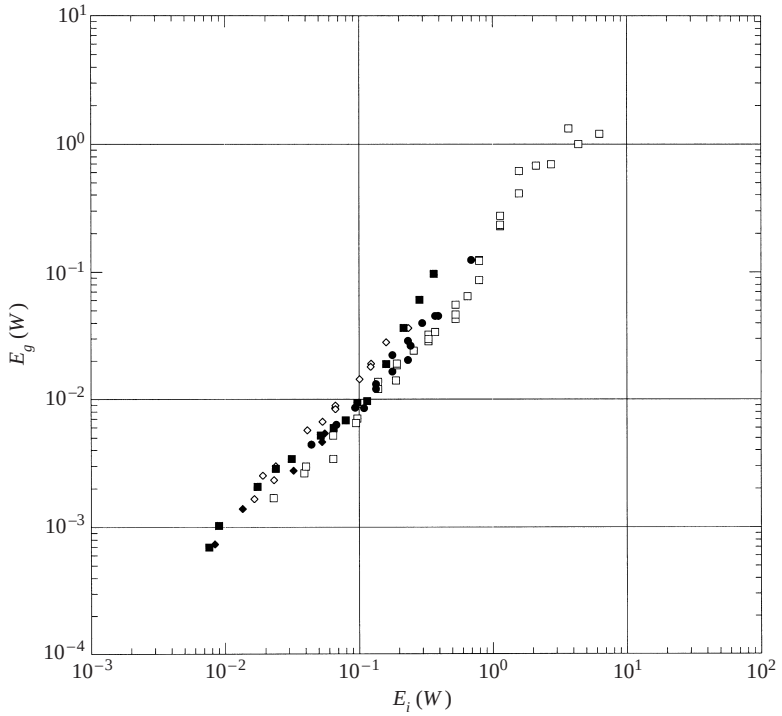

FIGURE 34. Comparison between the energy taken away by the drops per unit of time and the initial energy: ◆, ethanol $D_0 = 0.8\,\text{mm}$; ◇, water $D_0 = 0.8\,\text{mm}$; ■, ethanol $D_0 = 2.7\,\text{mm}$; □, water $D_0 = 2.7\,\text{mm}$; ●, water $D_0 = 5\,\text{mm}$.

According to equation (4.36), the diameter of the cusp at $\tilde{r} = 1$ is proportional to the injection diameter and is independent of the Weber number. This conclusion is consistent with the experimental observations reported in figure 15 where $S_{max} \simeq 0.13 D_0^2$. The drop diameter, is about twice the cusp diameter, which is the signature of a capillary instability. These conclusions do not hold when the drops are emitted before the edge of the cusp, which often occurs without forcing.

4.6. *Drop formation and size*

Several results obtained in the detailed study of the forced cusps are used in this section to analyse the transition from liquid sheet to drops when no forcing is applied to the liquid sheet.

Using the same method as presented in figure 32 to measure the ejection velocity of the drops v_d, we evaluate the energy E_g taken away by the drops per unit of time as

$$E_g \equiv n_g \left[\frac{\pi}{12} \rho d^3 v_d^2 + \pi d^2 \sigma \right], \tag{4.37}$$

where n_g is the number of drops emitted per unit of time, which can be evaluated with the conservation of mass as $n_g = \frac{3}{2} D_0^2 U_0 / d^3$. This energy can be compared to the initial energy per unit of time of the impacting jet $E_i \equiv \frac{1}{8} \pi \rho U_0^3 D_0^2$. This comparison is presented on figure 34 and reveals that the energy taken away by the drops per unit of time is of the order of 10% of the initial energy. A large amount of the initial energy is thus dissipated in the drop formation mechanism. Moreover, the ratio of the surface to kinetic energy of the drops shows that most of the drops energy

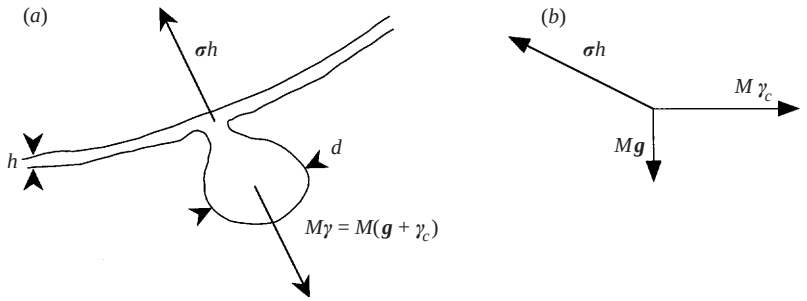

FIGURE 35. Sketch of drop detachment: (*a*) force balance at the point of drop detachment, (*b*) detail of the force balance.

is kinetic. These observations are consistent with G. I. Taylor's "About 98% of the kinetic energy therefore disappeared in the region where the drops were formed. A very small fraction of this energy was carried away in the form of surface energy of the drops, and all the rest must have been lost in turbulence within the drops." This conservation law approach is thus not appropriate to find the size of the drops.

From section § 4.5 we know that the travel time along the cusp τ_t is of the order of R/U_0. This time can be compared to the characteristic time of the Savart–Plateau–Rayleigh instability $\tau_{SPR} \approx \sqrt{\rho D_0^3/\sigma}$, based on the initial diameter D_0, that has been shown to be the order of magnitude of the rim. This comparison leads to the following ratio which shows that in the range $100 < We < 1200$, drops have time to form through that instability as they travel from the apex to the extremity of the cusp:

$$\frac{\tau_t}{\tau_{SPR}} \approx \sqrt{We} \gg 1. \tag{4.38}$$

As they move along the cusp, drops attached the liquid sheet of thickness e are given an acceleration $\boldsymbol{\gamma} = \boldsymbol{g} + \boldsymbol{\gamma}_c$ as indicated in figure 35(*b*), which that can be expressed using (4.34):

$$\gamma = g\sqrt{1 + \left[8\epsilon\left(\frac{a}{D_0}\right)^2\right]^2}. \tag{4.39}$$

From figure 33, the highest values of $\tilde{r_0} = 1-\epsilon$ which correspond to natural cusps are $\tilde{r_0} \in [0.85, 0.9]$ or equivalently $\epsilon \in [0.1, 0.15]$. This experimental observation implies that for natural cusps, 8ϵ is of order unity. In this limit equation (4.39) shows that the acceleration acting on the drops reduces to g when $D_0 \gg a$ and tends to $2\sigma/(\rho D_0^2)$, independent of g, for injection diameters smaller than the capillary length. The transition between these two regimes is sharp due to the fourth power in the ratio a/D_0. For this reason, only the two distinct limits are discussed below. At the point of detachment, the body force $\sim \rho d^3\gamma$ equilibrates the capillary attaching force $\sim \sigma h$ as sketched in figure 35. This physical model leads to the drop size evolution:

$$\frac{d}{D_0} \sim We^{-1/3} \quad \text{for} \quad D_0 \ll a \tag{4.40}$$

and

$$\frac{d}{a} \sim We_a^{-1/3} \quad \text{for} \quad D_0 \gg a, \tag{4.41}$$

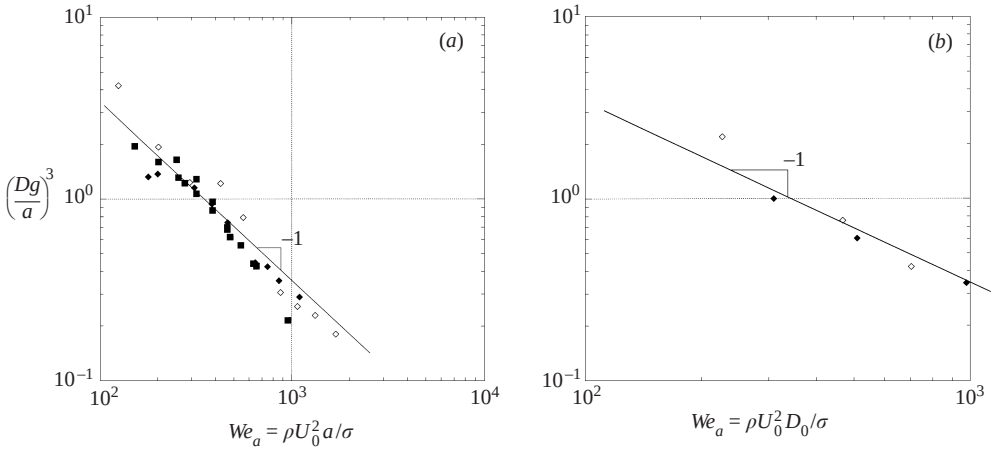

FIGURE 36. Comparison between the evolution predicted by the model and the drop diameter measured experimentally. (*a*) $D_0 \geqslant a$: ◆, ethanol $D_0 = 2.7\,\text{mm}$; ◇, water $D_0 = 2.7\,\text{mm}$; ■, water $D_0 = 5\,\text{mm}$; (*b*) $D_0 \leqslant a$: ◆, ethanol $D_0 = 0.8\,\text{mm}$; ◇, water $D_0 = 0.8\,\text{mm}$.

where $We_a \equiv \rho U_0^2 a/\sigma$. In the first limit where the injection diameter is smaller than the capillary length (4.40), the drop diameter is expected to be independent of g and to scale with D_0. In the opposite limit (4.41), the drop diameter predicted by this model is independent of D_0 and depends only on the capillary length of the liquid. This model is compared to the experimental results on figure 36, where equation (4.40) is used for the jets on figure 36(*a*) and equation (4.41) for the jet on figure 36(*b*). In the cusp domain considered, $100 < We < 1000$, figures 36(*a*) and 36(*b*) reveal a reasonable agreement between the model and the experimental measurements for the Weber number dependence. For the order of magnitude, figure 36(*a*) shows that $d \approx a$ for $D_0 \geqslant a$ and $d \approx D_0$ for $D_0 \leqslant a$. Both results are consistent with the model presented.

5. Conclusion

This paper is a study of smooth liquid sheets which form when a cylindrical jet impacts a disc of similar diameter, from the impact of the jet on the disc, to the stopping of the jet and the destruction of the sheet.

We first focus on the forcing mechanism needed to eject the impacting film horizontally and show that the initial momentum flux is altered by both the viscous stresses on the disc and by the lip action at the edge of the impactor.

A detailed study of the flow in the stationary liquid sheet is then presented where we prove that the film thickness evolves as the inverse of the distance from the impact point, and where the velocity in the film is shown to remain constant and equal to the velocity at the edge of the impactor.

Using these characteristics of the flow in the sheet, a force balance model is proposed to account for the maximal radial extension R. This model is shown to be in close agreement with the experimental results obtained in the range $We \in [100, 1000]$. For higher Weber numbers, the action of the surrounding air can no longer be neglected and the sheet does not remains smooth but oscillates like a flag. A detailed study of this flapping regime is reported in Villermaux & Clanet (2002).

A section is devoted to the dynamics of formation and destruction of the liquid

sheet. Even though the formation takes longer than the destruction, both phases develop on the characteristic time R/U_e, where U_e is the velocity of the liquid at the edge of the impactor.

The final part of the article focuses on the cusps observed in the stationary regime at the edge of the liquid sheet and on the drop formation mechanism. The study of the cusps reveals that their shape is close to a logarithmic spiral, the curvature of which is of the order of $1/R$. For the formation process of the drops, one observes that the drops form on the rim through a Savart–Plateau–Rayleigh instability, and then grow and propagate on the cusp prior to their detachment. During their propagation they are attached at the liquid film by capillary action and they are subject to both gravitational and the centrifugal acceleration. When the acceleration effect overcomes the attachment capillary force, the drops detach with a diameter that scales with D_0 in the limit $D_0 \leqslant a$ and with a in the limit $D_0 \geqslant a$. The thickness of the film that characterizes the strength of the attaching force imposes to the mean drop diameter, a $We^{-1/3}$ dependence. The general conclusion that can be applied to other atomization processes resulting from the transition from liquid sheet to drop is that the drop diameter results from a local equilibrium between the local accelerations and the local attaching forces.

We thank H. A. Stone and the three referees for their constructive criticisms of the original version of this article. We also thank Jacky Minelli and Serge Layat for the skillful technical assistance they provided on the experimental set-up.

REFERENCES

Bayvel, L. & Orzechowski, Z. 1993 *Liquid Atomization*. Taylor and Francis.

Becquerel, A. C. 1841 Funérailles de M. Savart. *Arch. l'Acad. Sci. Paris*, 1–10.

Bogy, D. B. 1979 Drop formation in a circular liquid jet. *Annu. Rev. Fluid. Mech.* **11**, 207–228.

Bouasse, H. 1923 *Jets, Tubes et Canaux*. Librairie Delagrave, 15 rue Soufflot, Paris.

Boussinesq, J. 1869*a* Théories des expériences de Savart, sur la forme que prend une veine liquide aprés s'être choquée contre un plan circulaire. *C. R. Acad. Sci. Paris* **69**, 45–48.

Boussinesq, J. 1869*b* Théories des expériences de Savart, sur la forme que prend une veine liquide aprés s'être heurtée contre un plan circulaire (suite). *C. R. Acad. Sci. Paris* **69**, 128–131.

Clanet, C. 2001 Dynamics and stability of water bells. *J. Fluid Mech.* **430**, 111–147.

Dombrowski, N. & Fraser, R. P. 1954 A photographic investigation into the disintegration of liquid sheets. *Phil. Trans. R. Soc. Lond.* A **247**, 101–130.

Dombrowski, N., Hasson, D. & Ward, D. E. 1960 Some aspects of liquid flow through fan spray nozzles. *Chem. Engng Sci.* **12**, 35–50.

Fraser, R. P., Dombrowski, N. & Routley, J. H. 1963 The filming of liquids by spinning cups. *Chem. Engng Sci.* **18**, 323–337.

Hinze, J. O. & Milborn, H. 1950 Atomization of liquids by means of a rotating cup. *Trans. ASME* : *J. Appl. Mech.* **17**, 145–153.

Huang, J. C. P. 1970 The break-up of axisymmetric liquid sheets. *J. Fluid Mech.* **43**, 305–319.

Kirchhoff, G. 1876 Vorlesungen über matematische Physik. *Forchheimer Hydraulik*, 341.

Lefebvre, A. H. 1989 *Atomization and Sprays*. Taylor and Francis.

Pandit, A. B. & Davidson, J. F. 1990 Hydrodynamics of the rupture of thin liquid films. *J. Fluid Mech.* **212**, 11–24.

Plateau, J. 1873 *Statique Experimentale et Theorique des Liquides*. Gauthier-Villars.

Savart, F. 1833*a* Memoire sur la constitution des veines liquides lancees par des orifices circulaires en mince paroi. *Ann. de Chim.* **53**, 337–386.

Savart, F. 1833*b* Memoire sur le choc d'une veine liquide lancée contre un plan circulaire. *Ann. de Chim.* **54**, 56–87.

Savart, F. 1833*c* Suite du Mémoire sur le choc d'une veine liquide lancée contre un plan circulaire. *Ann. de Chim.* **54**, 113–145.

Savart, F. 1833*d* Memoire sur le choc de deux veines liquides animes de mouvements directement opposs. *Ann. de Chim.* **55**, 257–310.

Squire, H. B. 1953 Investigation of the instability of a moving liquid film. *Brit. J. Appl. Phys.* **4**, 167–169.

Taylor, G. I. 1959*a* The dynamics of thin sheets of fluid. I Water Bells. *Proc. R. Soc. Lond.* A **253**, 289–295.

Taylor, G. I. 1959*b* The dynamics of thin sheets of fluid. II Waves on fluid sheets. *Proc. R. Soc. Lond.* A **253**, 296–312

Taylor G. I. 1959*c* The dynamics of thin sheets of fluid. III Disintegration of fluid sheets. *Proc. R. Soc. Lond.* A **253**, 313–321.

Villermaux, E. & Clanet, C. 2002 Life of a flapping liquid sheet. *J. Fluid Mech.* **462**, 341–363.

Watson, E. J. 1964 The radial spread of a liquid jet over a horizontal plane. *J. Fluid Mech.* **20**, 481–499.

Weihs, D. 1978 Stability of thin, radially moving liquid sheets. *J. Fluid Mech.* **87**, 289–298.